Packaging and Characterization of a NbTiN Superconducting Nanowire for the Design of an Optimal Nanowire Meander Structure

by

Antonio Scotland

A thesis
presented to the University of Waterloo
in fulfillment of the
thesis requirement for the degree of
Master of Applied Science
in
Electrical and Computer Engineering

Waterloo, Ontario, Canada, 2013

AUTHOR'S DECLARATION

I hereby declare that I am the sole author of this thesis. This is a true copy of the thesis, including any required final revisions, as accepted by my examiners.

I understand that my thesis may be made electronically available to the public.

Antonio Scotland

Abstract

The Superconducting Nanowire single-photon detector (SNSPD) made with niobium-titanium nitride (NbTiN) thin films fabricated on oxidized silicon substrates are highly promising nanodevices. The SNSPD is an immensely capable infrared single photon detector. When cooled down with liquid helium the device exhibits high detection efficiency, low dark-counts in spite of fast response times, and low timing jitter. For good single-photon sensitivity at telecom wavelengths, picosecod timing resolutions (<100 ps), and high counting frequencies, the SNSPD is first choice compared to the alternatives like indium gallium arsenide avalanche diode detectors, silicon single photon avalanche diode detectors, and other superconducting single photon technology like, transition edge detectors. These SNSPD characteristics make it ideal for long distance quantum key distribution (QKD).

Although the exploitation of the constructive interference that occurs at the SiO_2/Si interface can boost detector efficiency, efficient packaging and fiber coupling is often a limiting factor in the overall system quantum efficiency (SQE). In an attempt to maximize SQE, we use a controlled expansion alloy for optimal performance at cryogenic temperatures. This nickel-iron alloy has a high relative permeability and, therefore, attenuates electromagnetic interference. Our report focuses on the theoretical and experimental methods used in the characterization of an un-patterned NbTiN superconducting nanowire. We use simulations based on the gathered experimental data to design an optimal SNSPD meander and calculate its expected SQE. We also use simulations to analyze the speed and value added to secure key rates in long distance QKD schemes up to 400 km with down-conversion sources with positively spectrally correlated and decorrelated photon pairs at 1550 nm wavelength.

Acknowledgements

I will like to thank Dr. Hamed Majedi for his support as my supervisor, and for allowing the use of his lab facilities to carry out my experiments. In addition, I will like to thank Dr. Thomas Jennewein, for access to his lab equipment to complete my work. I consider myself fortunate to be a part of the IQC over the last two years, and I appreciate the support I have received from several members of the IQC. In particular, Roberto Romero has been a key point of support in getting my experiments prepared.

I would like to thank Harmen Van Der Heide of the Science Technical Services machine shop for his guidance and support in the fabrication of my packaging. I would also like to thank my readers Dr. Irene Goldthorpe and Dr. Thomas Jennewein for taking the time to review and evaluate this report. Finally, I would like to thank the IQC, its sponsors, and the University of Waterloo for their financial support.

Table of Contents

List of Figures

List of Tables

Chapter 1

Introduction

1.1 An overview of this thesis

In chapter 1, an overview of the most pertinent single photon detector properties are discussed. We also look into the most probably applications for the SNSPD design discussed in this report, beginning with long distance Quantum key distribution (QKD). In chapter 2, an overview of superconductivity, the hotspot detection model for the superconducting nanowire, along with the more pertinent characteristics of the super conductor that lays the foundation for any superconducting single photon detector (SNSPD) design are discussed such as, kinetic inductance, device geometry, fabrication, and structure, etc. In addition, we explore an electrical device model that simulates the photo response voltage pulse for the SNSPD.

Chapter 3 describes the preparation of the packaging and cryogenic dipper stick for the SNSPD. The many steps involved in the design and fabrication are discussed. The cost of use and adaptability of the packaging and dipper stick is also highlighted. We also discuss the issues with coupling a fiber to a single un-patterned nanowire. Next, an overview of DC screening and IV characterization of the device is explored, after device operation is confirmed at low temperatures by tracking the corresponding resistance levels.

In chapter 4 reports on the results of optoelectronic characterization of the superconducting nanowire. Optoelectronic characterization is performed at 1550 nm to gauge the detection efficiency at this wavelength keeping in mind the most likely application for the device. Also, an optical coupling model for single mode fiber coupled SNSPD is explored. Misalignment of the fiber is introduced into the coupling model to add a margin of error. We finally, simulate the system quantum efficiency of our desired meander structure based on acquired experimental data. In chapter 5, we conclude with our final design recommendation, and its likely advantages, along with key requirements for the most likely application of the device i.e. long distance QKD.

1.2 Properties of single-photon detectors

Any single-photon detector's performance can be assessed by its detection efficiency, count rate, dark count rate, dead time, and timing jitter. These parameters are defined in this section.

1.2.1 Detector efficiency

When a photon is absorbed by the single-photon detector a measurable amount of electrical energy is transmitted through the electrical connections. The event signifies the detection of at least one photon. The sensitivity of the detector, which may be controlled by a bias current, is directly related to the detector efficiency. In our case the detection efficiency is defined as the percentage of counts registered out of all photons that arrive at the detector.

The detection efficiency of the superconducting nanowire single photon detector (SNSPD) can also be affected by wavelength and polarization. The detector efficiency is generally higher for high energy photons, and the sub-wavelength dimensions of the superconducting nanowire make's it inherently sensitive to polarization. This polarization sensitivity can be a problem when the polarization of the incoming photons is not fixed as a SNSPD may have a biased detection probability for one polarization over another.

In addition, the system quantum efficiency (SQE) is a product of the inherent detector efficiency among other factors. The SQE of the SNSPD is defined as such, (**coupling efficiency**) x (**detector efficiency**). The degree coupling efficiency is a direct result of the effectiveness of the SNSPD packaging, and is the measure of the coupling between the photons leaving the fiber ferrule and the nanowire(s) present on the SNSPD surface[1].

1.2.2 Count rate

The count rate of a single-photon detector can be described as the number of single-photons detected per unit time[1]. Each detector has a maximum count rate that can be defined as the maximum number of photons that a detector can count per unit time at a given average detector efficiency. Note that if photons arrive at the detector at a rate higher than the maximum count rate, then the efficiency of the detector will decrease as photons will arrive outside the detection window of the detector and not be detected while others might be absorbed at a lower than average efficiency. This is known as saturation or afterpulsing. Of course the latter mentioned behavior of the saturated single-photon detector does depend on the detector technology employed. The most important factor in determining the count rate of a single-photon detector is the dead time. The inverse of the dead time gives a good estimate for the count rate of a detector[1].

1.2.3 Dark count rate

Dark counts are random false counts due to the material properties of the detector, the biasing conditions or contributions from external noise. Also known as noise, the dark count introduces a probability that a single-photon count may actually be a false count. The dark count is measured by the dark count rate (DCR). The DCR probability is calculated as such, (**dark count rate**)/ [(**detection efficiency** x **photon arrival rate)** + (**dark count rate**)]. One can see why detector efficiency and arrival rates are important in the presence of dark counts. The most important measurement for dark count is the one registered during an actual experiment because any dark counts registered while the detector is totally shielded can lead to a false sense of the expected dark count rate when implemented[1].

1.2.4 Dead time

The dead time of a single-photon detector is the time during which the detector cannot reliably register a second photon count. The factors that influence the measured value of the dead time vary from one detector technology to the next. A bias circuit or counting electronics accounts for the dead time measured in most cases. The maximum count rate of a single-photon detector is determined by the dead time. For the superconducting single-photon detector, the dead time is the sum of the rise and fall time of the voltage response of the device when a photon is absorbed. This dead time can be approximated as the fall time as the rise time is negligible in comparison[2].

1.2.5 Timing jitter

The jitter of a single-photon detector can be described as the uncertainty in the delay between when the photon is absorbed and when the device responds with an electrical pulse. The full half width maximum (FHWM) of the delay times give an approximation for the timing jitter of the detector. The distribution of delay times is usually a Gaussian distribution, whose shape varies due to the source of the jitter and detector type. The jitter, therefore, is the precision with which a single-photon detector can localize the arrival time of a photon[2].

1.2.6 Comparison of different single-photon detector technologies

Table 1, shows the comparison between the state of the art technologies in single photon detection at 1550nm wavelength. The table highlights and juxtaposes the most pertinent aspects of the detectors selected among the many currently available. A dimensionless figure of merit that takes in to account the detector efficiency, dark count rate, and timing jitter is used to holistically rank the different technologies in the table, the higher the figure of merit the better the single photon detector. This method of ranking is more apt that the use of noise equivalent power of the detectors because detectors that do not resolve photon numbers does not measure optical power. This means of justifying the overall effectiveness of the detector gives an idea of how much detector efficiency is on offer versus the dark count rate and timing jitter of the detector. This means ranking single photon detectors is well suited to applications such as Quantum key distribution, as the quantum bit error rate (QBER) is the ratio of DCR to sifted detected photon rate, which is the rate after comparing transmission and receiving basis[2]. The figure of merit, H, is given by,

$$H = \frac{\eta}{D\Delta t} \qquad (1.0)$$

Where

η = detector efficiency

D = Dark count rate (DCR)

Δt= timing jitter

Overall, the best vacuum and semiconductor technologies at near infrared have significantly greater dark counts at their respective operating temperatures than that of the superconducting detectors. This is because in the superconducting nanowire electrical noises and stray light are less of a contributor to a well packaged detector cooled down to 4.2 K or below. In addition, while the timing jitter for the best semiconductor detectors at near infrared is comparable to that of the superconducting detectors, with the exception of the Transition-edge sensors, the InGaAs avalanche photodiode (APD) detector is much more prone to dark count, which arises from the injection into the junction of charge carriers. This process can take place via thermal excitation, tunneling across the depletion zone, and emission by trapping centers[1][3]. The jitter is a major detracting factor in particular applications such as Quantum Key Distribution. The detection efficiency of the vacuum and semiconductor detectors may be comparable and higher to that of the superconducting detectors,

---

[1] Major cause of afterpulsing in the InGaAs semiconductor detector. Afterpulses are false counts that occur in the gated APD due to the remission of charges trapped during a previous avalanche.

but the amount of efficiency offered per unit of dark count and timing jitter is higher among the superconducting detectors, as shown in table 1.

Table 1: A comparison of the best of different types of infrared single-photon detector technology[4][1]

Detector type	***Vacuum tube***	***Semiconducting APD***		***Superconducting SPD***				
Detector	PMT[2](infrared)[2]	InGaAs (self-differencing)[5]	NFAD[3][6][7]	STJ[4][8]	TES[5][9]	Nb SNSPD[10], [11]	NbN SNSPD[12], [13]	NbTiN SNSPD[14], [15]
Detector efficiency @ 1550 nm	2.0%	10.0%	10.0%	17.0%	95%*	1.0%	10.0%	2.8%
Max. count rate (MHz)	10	100	100	0.005	0.1	150	1000	300
Dark count rate (KHz)	200	16	0.1	0	0	0.1	0.1	0.02
Timingjitter (FWHM), (ps)	300	55	60	-	1.00E+05	100	60	60
Wavelength (nm)	1700	1700	>1000	>2000	>2000	>1500	5000	>1500
Photon number resolution	Yes	Yes	No	Yes	Yes	No	No	No
Operating temperature (K)	200	240	193	0.25	0.1	2	2	2
Figure of merit	3.33E+02	1.14E+05	1.66E+07	-	-	1.00E+06	1.67E+07	**2.33E+07**

Notes: *These measurements took place in an optical cavity to maximize coupling efficiency

---

[2] Photomultiplier tube single photon detector

[3] The negative feedback avalanche diode single photon detector

[4] Superconducting tunneling junction single photon detector

[5] Transition edge sensor single photon detector

In particular, the Niobium based SNSPD has a very fast relaxation time, and hence response time. The use of niobium accounts for the superior count rate of the niobium based SNSPD. The NbTiN SNSPD is seen as the most superior of the SNSPDs, and this is because the optical properties of the substrate of the particular NbTiN SNSPD cited in table 1. Furthermore, NbTiN alloy allows for higher critical temperature than NbN and Nb. This allow for more practical operating temperatures. In addition, the lesser penetration depth leads to less parasitic inductances when compared to the Nb and NbN SNSPD[16].

1.3 Applications of single-photon detectors

Single photon detectors, have a myriad of applications. From Quantum key distribution (QKD), to CMOS device testing. This section emphasizes some the more recent and still developing applications of the single photon detector. This brief overview highlights the justification of further research in the area of developing the single photon detector technology, especially at infrared detection range.

1.3.1 Long distance fiber based Quantum Key Distribution (QKD)

The ideal detector for QKD in fiber is one in which the dark count rate and response time are approaching zero, while the detection efficiency at the wavelength of interest would be high[17]. For long distance transmission over fiber the ideal wavelengths are 1310 nm and 1550 nm. These wavelengths are selected because they offer the lowest level of attenuation per kilometer, and are thus most ideal for long distance transmission in fiber. Figure 1-1, gives a general idea of the relationship between attenuation and wavelength of transmission. It is important to note that most of the attenuation at the telecom wavelength range is due to Rayleigh scattering, where light interacting with particles of dimensions similar to the wavelength of incident electromagnetic radiation.

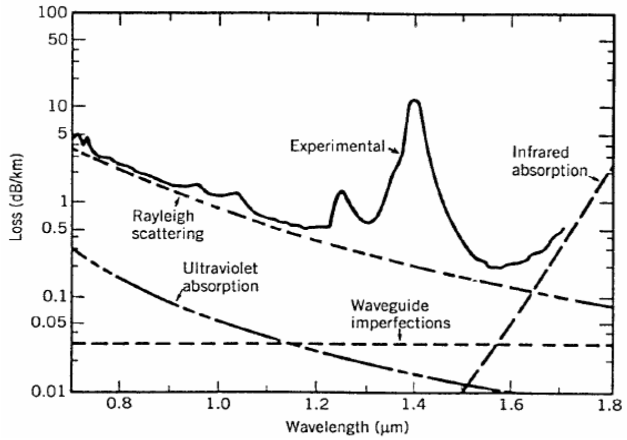

Figure 1-1: Attenuation versus transmission wavelength in fiber optic cable[18]

At telecom wavelength, over long distances gated InGaAs detectors are necessary to deal with the relative high dark count levels. In the case of the fiber coupled SNSPD, the polarization of light needs to be controlled. This is because SNSPD nanowire meanders are very sensitive to changes in polarization. Differences in polarization can lead to different photon absorption levels and hence different detector efficiencies for photons of different polarizations[12].

In addition, for QKD, the timing jitter of the single photon detector must be low, ideally less than 100 picoseconds (ps). The lesser this uncertainty in the responsiveness of the detector, the faster the source can be i.e. higher clock rates for arriving photons. A low jitter time also presents the option of having more frequent time stamping at the receiving end. In the context of the quantum bit error rate (QBER), when a high link loss is present, a low timing jitter, therefore, allows one to reduce the ratio of dark counts to detected photons per time bin. This ratio is a critical contributor to QBER at this point[19].

Typically, in QKD, quantum entanglement of polarized photons or another quantum state of the photon is used along with a particular communication protocol and quantum algorithm to exchange an encryption key. Any interception of the encryption key by an eavesdropper is made apparent by the quantum algorithm being used. Therefore, QKD allows, highly secure, key based transmission of information. One QKD scheme that is popular over shorter distances, because of the enhanced security inherent in the use of entangled photons, is the bi-partite quantum entanglement scheme[17]. However, in the case of long distance information transmission, entangled photons are difficult to synchronize. This is certainly the case in spontaneous parametric down conversion (SPDC). In quantum mechanics, the entangled photons are produced by a squeezing operator, which is itself a function of the Hamiltonian of the system, acting on the vacuum state of the photons coming from the source. This is the main mechanism by which photon pairs are produced.

This method not only induces a definite probability of producing higher order pairs that introduce a security weakness for potential hacking of encrypted information, but it typically produces photons of different wavelengths. In the case of long distance transmission schemes, spectrally uncorrelated photons move at different speeds in fiber optic cable, therefore, over long distances, entangled photons can arrive in different time bins i.e. the ability to localize the arrival of entangled photon pairs using single photon detectors is reduced. This makes it more difficult to implement any QKD protocol based on entangled photons.

One solution to the latter problem is to produce spectrally correlated entangled photons. This can be done by characterizing a SPDC source created through type II phase matching at 1550 nm using a Barium Borate (BBO) crystal. This source, as recently demonstrated, produces positive or no spectral correlations between photons. This allows for the production of fiber coupled photons with positive spectral correlation[20]. Note that the ideal protocol for a symmetrical source with polarization entangled photons is the BBM92 protocol. In the BBM92 protocol the source can produce photon pairs in the following entangled state:

$$|\boldsymbol{\psi}^{-} > = \frac{\mathbf{1}}{\sqrt{\mathbf{2}}}(|\boldsymbol{HV} > \; - |\boldsymbol{VH} >) \qquad (\mathbf{1.1})$$

After both recipients receive their photons, they measure in one of the two non-orthogonal basis i.e. H or V; where, H, represent horizontal polarization and, V, vertical polarization. After some period of time they communicate over a public classical channel the basis they measured in for each photon they received. Measurements in the same basis that yield anti-correlated results are saved and the others are discarded. This is an example of the sifting process using the BBM92 protocol. The sifted results are converted to binary as follows $|H >$ to bit 0 and $|V >$ to bit 1. Then bob inverts his anti-correlated bit string to match that of Alice. This gives the raw key. The secure key rate comes after classical error correction is performed on the raw key to remove errors due to small imperfections. The upper limit QBER for this scheme is given by Gisen et al. [17];

$$\boldsymbol{I}(\boldsymbol{A},\boldsymbol{B}) = \mathbf{1} + \boldsymbol{elog_2}(\boldsymbol{e}) + (\mathbf{1}-\boldsymbol{e})\boldsymbol{log_2}(\mathbf{1}-\boldsymbol{e}) \qquad (\mathbf{1.2})$$

Where recipient A and B share mutual information with corresponding error rate, e, defined by equation 1.2. This equation can be thought of as the mutual dependence of the random information sent to each recipient. There also exists mutual information between the eavesdropper, E, and recipient A or B, that is;

$$\boldsymbol{I(A,E) = I(B,E) = \frac{2}{ln2}e + O\left(e^2\right) \approx \frac{2}{ln2} \cdot e} \qquad (\mathbf{1.3})$$

The maximum mutual information between the recipients must exceed that of any one eavesdropping on the communication taking place between the recipients; otherwise the creation of a secure key is impossible. This point at which $I(A,B) = I(A,E)$ is found to be at a 14.6% error rate[17]. Beyond a 14.6% QBER the amount of mutual information between and eavesdropper and either recipient would exceed the amount of mutual information between the recipients themselves. Finally, note that it is possible for an eavesdropper to employ a strategy wherein only a percentage of useful information shared between the recipients is stolen such that the QBER remains below 14.6%. In this case, the recipients must perform what is known as the privacy amplification protocol on the error-correlated key to reduce the maximum potential information the eavesdropper might gain to a very small value[17].

1.3.2 Simulation of a QKD setup with correlated entangled photon source based on current available technology

Recently, a QKD scheme in which an entangled source is symmetrically placed to achieve long distance exchange of encrypted information with up to 70 dB loss in fiber optic cable was proposed[6]. The source to be used in this system was characterized using an ID-201 InGaAs and negative feedback avalanche diode single photon detector (NFAD), shown in figure 1-2.

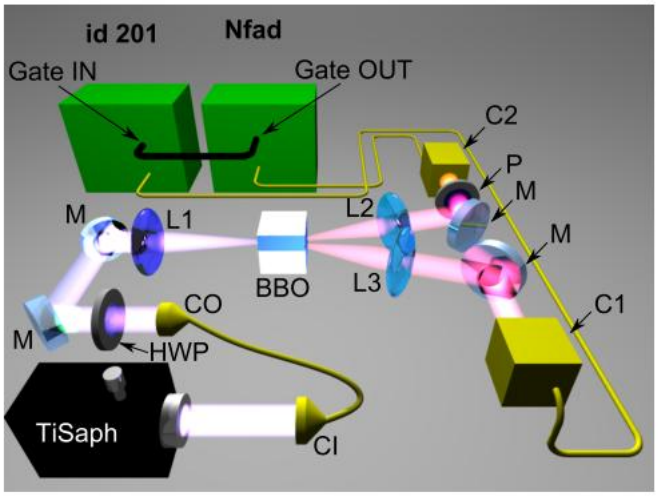

Figure 1-2: A fiber couple Ti:Sapphire laser is sent through single mode fiber using a coupler (CI), the output is then collimated (CO). The polarization is adjusted using a half-wave plate (HWP) and a lens (L1) focuses the beam of radius 150 μm entering the BBO crystal. Through SPDC, entangled photons are produced at an angle of 3°, which are then collected by plano-convex lenses L2 and L3 each with a focal length of 150 mm, and the coupling aspheric lenses C1 and C2 each with focal length 15.4 mm.[20]**.**

The following simulations in figure 1-3 demonstrate the testing of stipulated system in which an NFAD and SNSPD single photon detectors are used to detect the arrival of entangled single pairs of photons over long distances. The optical losses in each arm of the system are presumed to be equal. The NFAD is set at 8% detection efficiency with 100Hz DCR and after pulsing of 4%. The packaged SNSPD meander is set at 2.8% system efficiency with a 20Hz DCR and zero afterpulsing. The high responsiveness of the NFAD and SNSPD allows a maximum time coincidence time window of 100 ps. The initial loss, before transmission of information through fiber, due to coupling losses and free space losses is set to -13dB. No losses from analyzer equipment are considered.

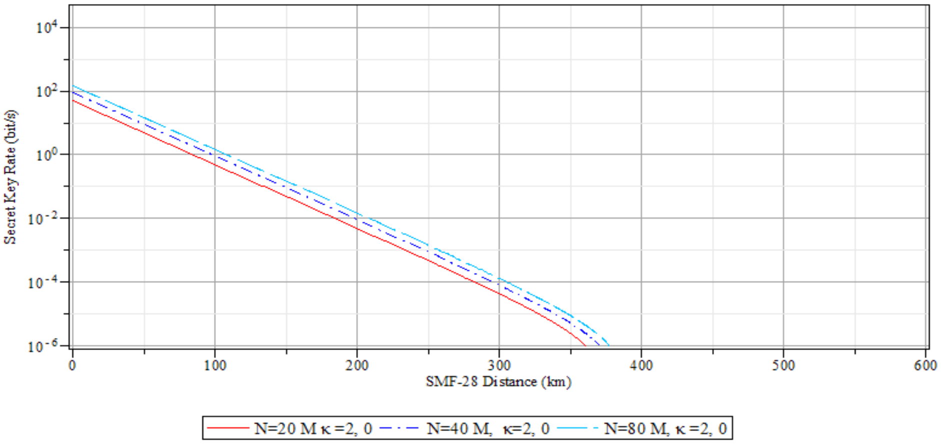

Figure 1-3: Simulation of secure key rate versus distance in SMF-28 fiber for a QKD scheme with a symmetrical, spectrally correlated source simultaneously using an NFAD and SNSPD at either end of the symmetrical quantum channels for entangled single photon detection. The secure key rate is plotted for BBO crystal photon pair generation, N at 20 MHz, 40 MHz, and 80 MHz. After pulsing, *κ*[6], is set at 4% for the NFAD and 0% for the SNSPD.

---

[6] ***κ***, is after pulsing of photons arriving outside the detection window that are absorbed at a lower than average efficiency

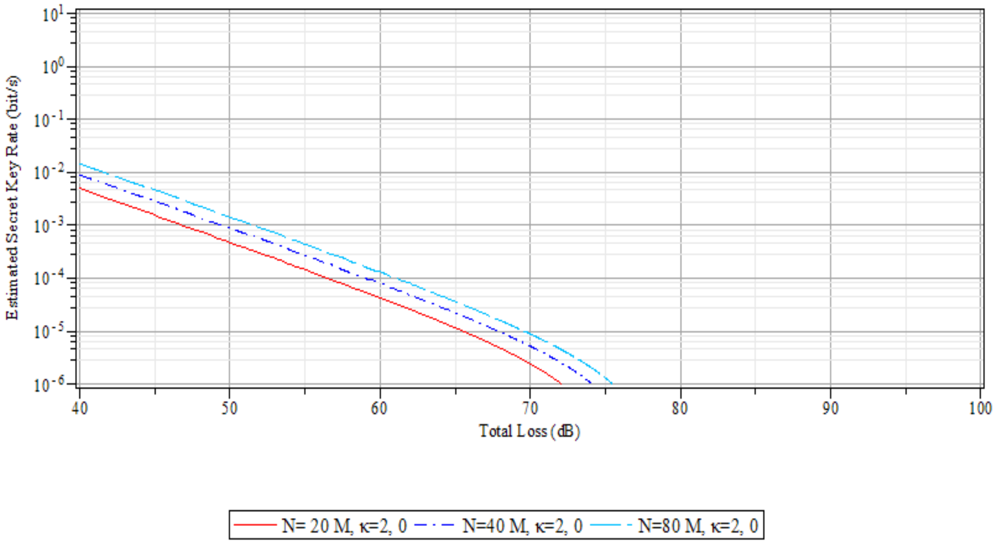

Figure 1-4: Simulation of secure key rate versus fiber attenuation (dB) for the same experimental setup highlighted in figure 1-3.

The quantum bit error rate (QBER) of this QKD scheme is a model based on optical visibility. The total quantum correlation visibility can be viewed a function of accidental visibility due to uncorrelated photon counts and dark counts in the time window. In addition, systematic errors introduced by source misalignment and other factors, such as the presence of a polarization analyzer, lead to the value of system visibility [21]. The quantum bit error rate and secure key rate are a function of these latter error sources and these relationships are thoroughly described by Ma *et a.* [22]. The quantum bit error model used in these simulations is similar to the one recently used by Yan *et al*[6], where the total effective detection efficiencies of the NFAD and SNSPD detectors is a function of channel losses, receiver optical loss, and finite detector efficiency. Therefore, the total effective detection efficiency decreases exponentially with distance in fiber. The QBER is given by equation 1.4.

$$\boldsymbol{QBER = \left[1 + \frac{\eta_A \eta_B}{\mu_P \left\{(1+\kappa_A)\eta_A + \frac{D_A}{N}\right\}\left\{(1+\kappa_B)\eta_B + \frac{D_B}{N}\right\}}\right]^{-1}} \qquad (\mathbf{1.4})$$

Where,

η_A, η_B – Effective detection efficiencies

μ_P - The rate of emission of the average photon pair = N x time window(w)

κ_A, κ_B – Afterpulsing of the detectors.

D_A, D_B – Represent the DCR for the respective detectors

N - Average photon pair generation rate in the BBO crystal

Based on equation 1.4, the lower bound for the secure key rate is calculated as follows;

$$\boldsymbol{R \geq \frac{1}{2}\{N\eta_A\eta_B[1 - f(QBER)H_2(QBER) - H_2(QBER)]\}} \qquad \boldsymbol{(1.5)}$$

Where,

$H_2(x) = -xlog_2(x) - (1-x)log_2(1-x)$; is the binary entropy function

$f(QBER) = 1.22$; is the correction factor in QKD

R- Lower bound for the secure key rate

The term $N\eta_A\eta_B$ represents the coincidence detection probability between recipient A and B. The correction factor is necessary because of the fact that practical error reconciliation protocols do not perform well when the theoretical maximum information transfer rate of the channel, for a particular noise level, is reached. This is also known as the Shannon limit. These simulations assume an optical fiber loss of 0.2 dB/km, and stipulate secure encryption of data of up to 300 km i.e. 150 km in either direction of the symmetrical source. Note that with a minimum source rate of just 20 MHz to achieve this distance in fiber with relatively higher secure key rate, the security estimated here is purely ideal as higher order pair generation is sure to occur at such high rates. Ironically, much higher source rates are necessary to prove QKD over these distances. Furthermore, even though the time window in these simulations is set at 100 ps, in reality the time tagger used to time stamp photon pair arrivals could pose as a bottleneck in this setup if the timing resolution of the time tagger is not appropriate ($\leq 100\,ps$).

1.3.3 Characterization of a single photon sources

The quantum dot is one example of a single photon source. In characterizing such a source the SNSPD does show its advantages over the avalanche photodiode detector single photon detector. For example, in measuring the spontaneous emission lifetime of the quantum dot, one can take advantage of the typically greater time resolution of the SNSPD. The greater responsiveness and ability to cope with high clock rates makes it ideal[23]. In addition, in carrying out quantum correlation measurements for a true entangled photon source, the superconducting single photon detector detector’s excellent time resolution again comes into play as the ability to time stamp at a high rate photon pair arrivals from fast entangled sources enhances your ability to verify correlation through precise localization of arriving photons[24].

1.3.4 Other applications

In the realm of communications technology, through the arrival times of single photons, information can be transmitted using a technique known as Pulse Position Modulation (PPM)[1]. The ability of a single photon detector to precisely localize the arrivals means that information can be sent at very high rates using very little power in a PPM scheme. This form of communication is ideal long distance free space communication, especially with receivers in outer space. The transmission of information at gigabit rates has already been proven at the telecom wavelength of 1550 nm. This was done using the SNSPD[25].

In addition, integrated circuit testing is another important application of the single photon detector. In particular, the SNSPD can be used to debug and diagnose chip failure in complementary metal oxide semiconductor (CMOS) devices. The release of energy during switching caused by the driving of electrons to higher energy levels when the field effect transistor reaches saturation mode leads to photon emission as the electrons lose this energy. These emitted photons are usually in the near infrared region, and the ability to detect these photons allows one to study the timing parameters of the CMOS device[26].

1.3.5 Most ideal infrared single photon detector choice for quantum information applications

The various applications outlined in section 1.2 all require similar single photon detector characteristics. Whether it is long distance QKD, single photons source characterization or CMOS chip testing, high detector efficiency with the ability to localize single photon arrivals to a high degree of precision and low dark count is what’s required in most applications. Table, 1, clearly shows that the NbTiN detector ranks number one in terms of the amount of system quantum efficiency (SQE) that is offered per unit of dark count and timing jitter. Therefore, the NbTiN detector with at least the parameters outlined in Table 1 is the ideal choice.

As one of the most likely applications for any optimal meander structure and packaging outlined in this report, QKD and the performance of the latter QKD scheme based on optical visibility will depend heavily on changes in the three key parameters of the figure of merit. For example, the amount of jitter in the system limits the time window that one can set for time stamping arriving photons. As previously mentioned, the total quantum correlation visibility can be viewed a function of accidental visibility due to uncorrelated photon counts and dark counts in the time window. Therefore, decreasing the time window will decrease contributions to the QBER in each sampling period (time window), that is, dark counts and uncorrelated photon arrivals. However, timing jitter of (< 100ps) is very consistent in SNSPD fabrications.

Therefore, it can now be easily seen how increases in the dark count of the packaged NbTiN SNSPD will be one of the most likely causes of corresponding increases in the QBER. The other most likely cause of significant increase in the QBER will come from any variation in the system quantum efficiency of the NbTiN SNSPD. As the SQE varies the total effective efficiency in the latter mentioned QKD model changes. This results in changes in the total quantum correlated visibility. In fact, any decrease or increase in the total effective efficiency has the largest unmitigated impact on the QBER as dark counts and after pulses can be obviously mitigated by decreasing the time window and increasing the entangled photon pair generation rate, N, in the BBO crystal.

The variation of QBER with system quantum efficiency and DCR of the SNSPD versus the ideal desired settings for the NFAD technology and entangled single photon source over ultra long distance (~ 400 Km) can be seen in Appendix A. Appendix A also gives a simulated minimum optimum NbTiN SNSPD efficiency and dark count rate with respect to the QBER and upper bound for the worse case settings of the SNSPD. The minimum optimum rate was found to be at least 5.103% system quantum efficiency with a dark count rate less than or equal to 61 counts per second for the packaged NbTiN SNSPD. The upper bound for the worse case settings of the SNSPD was found to be at least 6.989% efficiency with less than 326 dark counts per second. Therefore, our packaging and optimal meander structure should deliver at most a DCR of 61 CPS and SQE of at least 6.989%; this will provide performance superior to the current state of art in NbTiN SNSPD technology.

Chapter 2

Device operation, modeling and fabrication

2.1 Superconducting nanowire single photon detector operation

2.1.1 Superconductivity review

The phenomenon of superconductivity occurs when materials cooled down below their critical temperatures exhibit exactly zero resistance along with the expulsion of magnetic fields from within the material. This expulsion of magnetic fields as the material transitions to sub-critical temperature conditions is otherwise referred to as the Meissner effect. This effect characterizes the phenomenon as more than just perfect conductivity in classical physics. The main mechanism behind this effect is an induced surface current in the presence of a magnetic field that in turn nullifies the applied magnetic field in the core of the superconductor. These surface current increases to some maximum that corresponds to the critical screening current applied to the material. Beyond this critical screening current, the conductor ceases to be a superconductor.

As the temperature is lowered, the electrical resistivity of a metal conductor reduces. This reduction in temperature varies in different metals as crystal structures, substrates, impurities, and other factors come into play. Note that as normal conductors approach absolute zero temperatures they still exhibit some level of impedance to current flow. However, superconductors exhibit zero resistance as the temperature reaches below the critical temperature of the superconductor. Therefore, an electrical current made to flow in a superconductor below its critical temperature will flow indefinitely.

Some of the notable physical properties of superconductors include, their response to a magnetic field, critical temperature, and critical current at which the conductor is no longer superconducting. The type-I superconductor exhibits superconductivity below some single critical applied field and type-II have two critical fields between which they allow some penetration of magnetic fields within the conductor core. Moreover, in the field of single photon detector technology, the application of a bias current to a superconductor just below the critical current value allows it to return to its normal state when a photon is absorbed. The sudden transition is exploited as a photon detection mechanism.

There are two main theories that try to explain the phenomena of superconductivity. One is the Ginzburg-Landau theory, purely mathematical in nature and developed in 1950. It is a phenomenological model which describes type-I superconductors. The other is the BCS theory, which is a microscopic theory that proposes that electrons in most conventional superconductors form pairs, known as cooper pairs. These pairs have lower energy than the Fermi level i.e. the hypothetical level of potential energy for an electron in a crystal lattice.

2.1.2 Detection mechanism- The hot spot model

We have already explored some of the benefits that the superconducting devices have over there semiconductor counterparts. We will now explore in more detail the microscopic mechanism at play that make the superconducting devices better. When one examines the superconducting energy gap, 2Δ, we find that it is indeed up to three times lower than that of the semiconductor. As a result, when photons are absorbed by a superconductor based single photon detector, they can create a larger number of excited carriers. In figure 2-1, we see the depiction of this process. The subsequent non equilibrium generation and relaxation of quasiparticles upon absorption of a photon with energy, hv, begins with the excitation of a single member of the cooper pair whose energy is closest to that of the incident photon. The other member of the pair is left as a low energy quasiparticle. This is because the physical size of a cooper pair is much larger relative to the incident photon. This process is called the thermalization process. Next, the excited quasiparticle then goes on to quickly lose its energy. This rapid lose takes place during a few femtoseconds and can be attributed to electron on electron (e-e) scattering and the creation of newly excited electrons through secondary collisions. This process will continue until the mean energy of the quasiparticles is approximately the Debye energy (0.1 eV). This latter process constitutes the quasiparticle recombination process. At this point the quasiparticles lose their remaining energy via the emission of phonons (e-ph). The subsequent phonon emission leads to breaking of further cooper pairs. The avalanche created by this process eventually decrease back to the energy gap, 2Δ, however, the number of electrons increases to approximately, $\frac{hv}{2\Delta}$, and the effective electron temperature increases thus resulting creation of a hotspot; superconductivity is suppressed in this region. The process time $\tau_R + \tau_B + \tau_{es}$ can be as low as 10s of picoseconds. The process is depicted in figure 2-1[27].

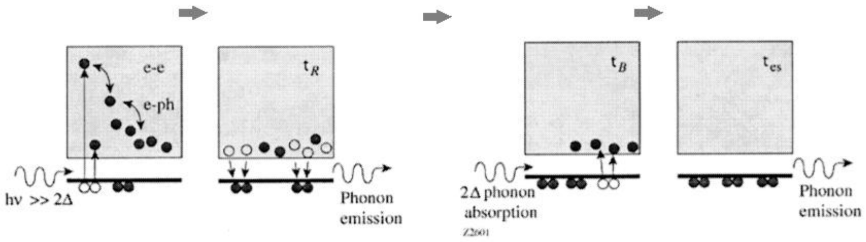

Figure 2-1: The photoresponse process of a superconductor excited by a photon. From left to right we see first the thermalization process, second the quasiparticle recombination process, third the breaking of pairs by phonons, and finally phonon escape to substrate. The box represents energy levels above the energy gap 2Δ while the dark line represents the transition point to the latter mentioned energy levels [27]**.**

However, note that the creation of the hotspot is not enough to form a resistive barrier as the size of the hot spot created is small relative to the size of the conductor. It's also essential that the superconducting material be current biased near its critical current. Upon creation of the hotspot current that once flowed through the former superconducting region is expelled to the sidewalks of the conducting strip. At this point the sidewalk current exceeds the critical current of the device. As a result, the electric field due to the increased side walk current is now able to penetrate the core of the outer region of the conducting stripe; this results in a voltage pulse. It is this voltage pulse that signifies that absorption of a photon[28]. Because of joule heating, the resistive barrier eventually covers the entire width of the nanowire before subsiding[26]. The voltage pulse generated is less than 1mV in magnitude and must be amplified to be tracked by readout electronics. Figure 2-2 depicts the resistive barrier formation on a stripe of effective width, w_e.

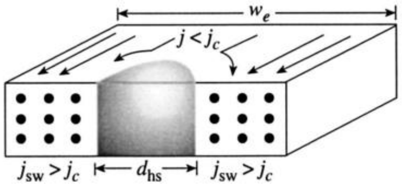

Figure 2-2: Formation of the resistive barrier of width, d_{hs}, across a stripe of superconducting material that is current biased near it's critical current, j_c , and sidewalk current, J_{sw}, in the single photon regime. The resistive barrier eventually covers the entire width of the nanowire before subsiding[28]**,**[26]

2.1.3 Kinetic inductance in a superconductor (one–dimensional)

The kinetic inductance of the superconducting nanowire plays an important role the electrothermal response and timing jitter; discussed in sections 2.1.5 and 2.1.7. Electrothermal response and timing jitter are key in potential applications such as QKD. Therefore, it is important to examine the nature of this inductance in detail.

Kinetic inductance is an equivalent series inductance caused by the inertial mass of mobile charge carriers in alternating electric field. Kinetic inductance is of great interest in nanowires. One implication of this inductance is the property of latching that affects the performance of the SNSPD. In normal metals the kinetic inductance can be derived beginning with the Drude model of transport[1][29].

$$\vec{J} = \sigma_e \vec{E} \qquad (2.1)$$

$$\vec{J} = \frac{n_e e^2 \tau_e}{m_e(1 - i\omega\tau_e)} \vec{E} \qquad (2.2)$$

Where,

$\vec{J}$ – current density

$\vec{E}$ – electric field

σ_e – complex conductivity of electrons

ω – angular frequency of the oscillating field

τ_e – elastic scattering time for an electron in a metal

n_e – electron (charge carrier) density

e – electron charge

m_e – electron mass

Now, in ohmic transport $\omega\tau_e \ll 1$ is typical and so the imaginary part of the conductivity is negligible and so ohm's law can be shown to be a result[1]. At very high frequencies, $\omega\tau_e \gg 1$ and so there exists a purely imaginary impedance. As a results,

$$\vec{E} = i\omega\left(\frac{m_e}{n_e e^2}\right)\vec{J} \qquad (2.3)$$

Now, consider a superconducting strip of width, ω_e , and thickness d_e, where both the width and thickness are less than the magnetic penetration depth of the material, λ, and the coherence length, ξ[1]. In such a strip, uniform supercurrent density can be assumed. As a result, kinetic inductance, L_k , of the strip can be obtained by making the following assumptions: , $\omega\tau_e \gg 1$, but $\tau_e \rightarrow \infty$ and $\omega \rightarrow 0$. The mass considered now becomes the mass of a cooper pair, $2m_e$, with cooper pair density, n_s, and collective charge, $2e$. Therefore equation 2.3 becomes;

$$\boldsymbol{L_k = \left(\frac{m_e}{2n_s e^2}\right)\left(\frac{l_d}{A_{cs}}\right)} \qquad \mathbf{(2.4)}$$

Moreover, n_s is dependent on temperature and current dependent in a superconductor. This dependence is expressed as,

$$\boldsymbol{n_s(T) = n_s(0)\left(1 - \frac{T}{T_c}\right)} \qquad \mathbf{(2.5)}$$

Where,

T − temperature

$\mathrm{T_c}$ − critical temperature of the superconductor

To find, n_s, dependence on current we turn to the Ginzburg-Landau theory, where for NbTiN superconducting nanowires this model is presumed to remain valid in range, $\frac{T_c}{2} < T < T_c$. If each parameter is assumed to vary with temperature and electron temperature is constant while current changes adiabatically with the relaxation times for quasiparticles and cooper pairs, then the superconducting order parameter can be expressed as[30];

$$\boldsymbol{\psi(r) = |\psi| e^{i\phi(\vec{r})}} \qquad \mathbf{(2.6)}$$

Where, the strip thickness $d_e \sim |r|$, $|\psi|^2 = n_s$, and ϕ is the phase. As a result, the current can be expressed as;

$$\overrightarrow{\boldsymbol{J_s}} = \frac{\boldsymbol{e}}{\boldsymbol{m_e}}|\boldsymbol{\psi}|^2\left(\hbar\nabla\boldsymbol{\phi}(\boldsymbol{r}) - \boldsymbol{2e}\overrightarrow{\boldsymbol{A}}\right) = \boldsymbol{2e}|\boldsymbol{\psi}|^2\frac{\hbar\boldsymbol{k}}{\boldsymbol{2m_e}} = \boldsymbol{2e}|\boldsymbol{\psi}|^2\boldsymbol{v_s} \qquad (\mathbf{2.7})$$

Where,

$A - vector\ potential$

$v_s - velocity\ of\ the\ cooper\ pairs$

When the cross sectional area of the nanowire is much less than the penetration depth, λ of the superconductor, then the contribution of the screening magnetic field can be considered negligible in calculating the free energy[1][31]. As done by Tinkham [31],

$$|\boldsymbol{\psi}|^{\mathbf{2}} = \boldsymbol{n_0}\left(\mathbf{1} - \left(\frac{\boldsymbol{\xi}(\boldsymbol{T})\boldsymbol{m_e}\boldsymbol{v_s}}{\hbar}\right)^2\right) \qquad (\mathbf{2.8})$$

Therefore,

$$\overrightarrow{\boldsymbol{J_s}} = \boldsymbol{2en_0}\left(\mathbf{1} - \left(\frac{\boldsymbol{\xi}(\boldsymbol{T})\boldsymbol{m_e}\boldsymbol{v_s}}{\hbar}\right)^2\right)\boldsymbol{v_s} \qquad (\mathbf{2.9})$$

Where n_0 is the cooper pair density at $T = I = 0$. Letting , $\gamma = kl_d$, where k is the magnitude of the superconducting wave number, and γ is the phase difference along the nanowire and is independent[1]. This yields;

$$\boldsymbol{I_s} = \frac{\boldsymbol{e}\hbar}{\boldsymbol{m_e}}\left(\frac{\boldsymbol{A_c}}{\boldsymbol{l_d}}\right)\boldsymbol{n_0}\left(\boldsymbol{\gamma} - \frac{\boldsymbol{\xi}^2\boldsymbol{\gamma}^3}{\boldsymbol{l_d}^2}\right) \qquad (\mathbf{2.10})$$

Where,

$A_c -\ cross\ sectional\ area$

$I_s -\ supercurrent$

Note that γ is related to L_k by the current-phase relation (CPR). Referring to the adiabatic approximation of time-dependent quantum mechanics, the Hamiltonian is given as[1]:

$$\boldsymbol{H = T + U(T)} \quad \boldsymbol{(2.11)}$$

Where,

$$\boldsymbol{U(T) \approx U} \qquad \boldsymbol{(2.12)}$$

Therefore,

$$\boldsymbol{\frac{2eV}{\hbar} = \frac{d\,\gamma}{dt}} \qquad \boldsymbol{(2.13)}$$

Now,

$$\boldsymbol{V = L_k \frac{d\,I_s}{dt}} \qquad \boldsymbol{(2.14)}$$

Hence,

$$\boldsymbol{L_k = \frac{\frac{\hbar}{2e}\frac{d\,\gamma}{dt}}{\frac{d\,I_s}{dt}} = \frac{m_e}{2e^2}\left(\frac{l_d}{A_c}\right)\left(\frac{1}{n_0\left[1 - \frac{3\xi^2\gamma^2}{{l_d}^2}\right]}\right)} \qquad \boldsymbol{(2.15)}$$

Since magnetic penetration depth , $\boldsymbol{\lambda^2(T) = \frac{m_e}{\mu_0 n_s(T) e^2}} \quad \boldsymbol{(2.16)}$

This implies;

$$\boldsymbol{L_k = \frac{\mu_0\lambda^2}{2}\left(\frac{l_d}{A_c}\right)\left(\frac{1}{n_0[1 - 3k^2\xi^2]}\right)} \quad \boldsymbol{(2.17)}$$

Again from Tinkman [31] and equation 2.17 derived previously we have;

$$\boldsymbol{I = \frac{3\sqrt{3}}{2} I_c\left(\xi k - k^3\xi^3\right)} \qquad \boldsymbol{(2.18)}$$

$$\boldsymbol{L_k = \frac{\mu_0 \lambda^2}{2}\left(\frac{l_d}{A_c}\right)\left(\frac{1}{n_0[1-3k^2\xi^2]}\right)} \qquad (\mathbf{2.19})$$

For $I \ll I_c$ equation 2.18 becomes,

$$\boldsymbol{\frac{I}{I_c} = \frac{3\sqrt{3}}{2}\,(\xi k)} \qquad (\mathbf{2.20})$$

One approximation for kinetic inductance can be seen as,

$$\boldsymbol{L_k \approx \mu_0 \lambda^2 \left(\frac{l_d}{A_c}\right)\left(\frac{1}{\left[1-\frac{4}{9}\left(\frac{I}{I_c}\right)^2\right]}\right)} \qquad (\mathbf{2.21})$$

When $\frac{4}{9}\left(\frac{I}{I_c}\right)^2 \ll 1$ we use the binomial expansion to arrive at [32];

$$\boldsymbol{\frac{L_k(I)}{L_k(0)} \approx \left(1+\frac{4}{9}\left(\frac{I}{I_c}\right)^2\right)} \qquad (\mathbf{2.22})$$

Similarly, after equation 2.18 is expanded into a Taylor series, an approximation for kinetic induction variation with current can be found as $I \to I_c$ as follows;

$$\boldsymbol{\frac{L_k(I)}{L_k(0)} \approx \left(\frac{1}{2\left(\frac{2}{3}\left(1-\frac{I}{I_c}\right)\right)^{\frac{1}{2}}}\right)} \qquad (\mathbf{2.23})$$

We see the following relationship between bias current and kinetic inductance for the nanowire in figure 2-3.

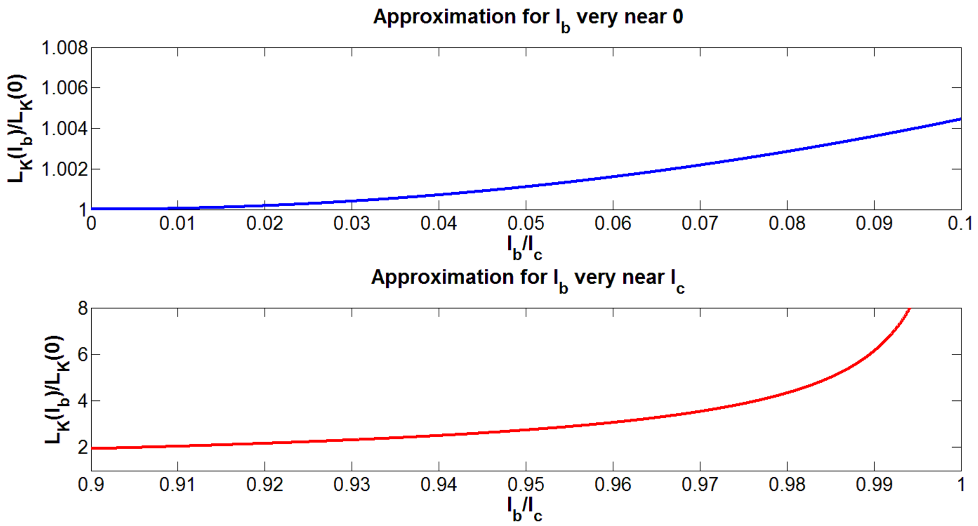

Figure 2-3: Analytical approximation for the current dependence of L_k optimized for bias currents, I_b near 0 (top plot) and near the critical current, I_c (bottom plot).

2.1.4 Estimation of Kinetic inductance in a nanowire

To estimate an average value for the kinetic inductance of a nanowire we refer to equation 2.21. At zero current and temperature, L_k will be at its minimum; at this point the equivalent relation would be,

$$L_k \approx \left(\frac{\mu_0 \lambda^2}{2}\right)\left(\frac{l_d}{A_c}\right) \qquad (2.24)$$

Therefore, the kinetic inductance per unit length can be found for different nanowires. For NbTiN nanowire with $A_c = 8 \times 10^{-16} m^2$, and $\lambda \approx 200\ nm$[16]. We get an approximate value for kinetic inductance for our nanowire of 31.5pH/µm.

2.1.5 Detection efficiency limitations

The chance of an incident photon forming a hotspot region on a nanowire expresses the probability of detection of that photon. The chance of the latter can be reduced by intrinsic factors and external factors. The intrinsic factor of major concern is whether an absorbed photon will lead to a hotspot on the nanowire. Indeed, the probability of absorbing a photon can be augmented by the use of an optical resonant cavity in which the photons essentially oscillate until absorbed. However, absorbing a photon does not necessarily mean a hotspot will be formed. In fact, the probability that a resistive hotspot is formed after photon absorption is also heavily dependent on operating temperature, bias current, and energy of the absorbed photon[33],[34],[35],[36],[37]. Moreover, the hotspot model previously discussed in section 2.1.2, indicates that at some bias current exceeding the critical current and at a point significantly below the critical current of the superconducting nanowire, there will be a cutoff of hotspot formation. However, in practice hotspots are still formed at currents well below the critical current. In addition, hot spot formation drops off exponentially after the critical current is exceeded; there is no hard cutoff point. Furthermore, the detection efficiency and bias current relationship becomes even more weakened for higher energy photons.

In addition, electro thermal feedback in superconducting nanowires does play a role in photon detection efficiency. If the kinetic inductance of the nanowire is reduced by increasing the cross-sectional area of the wire or reducing the nanowire length beyond some threshold point wherein the electrical response of the nanowire increases to the point where electro thermal feedback becomes stable, then the detection efficiency reduces. The best mode of operation for the nanowire is when the electro thermal response is unstable. A stable electro thermal response results in what is known as latching; where the wire is locked in a resistive state and can no longer detect photons[38].

The main external factor that mitigates detection efficiency is the absorptivity of the nanowire. This, of course, depends on the geometry of the nanowire and the optical properties of the thin film. One way to increase detection probability is by forming a nanowire meander pattern of area greater than the square of the wavelength of incident photons. Figure 2-4, demonstrates such a NbTiN nanowire meander pattern. However, there is a strong polarization dependence that affects the probability of absorption at different polarizations. For maximum absorption, the polarization of the incident photon should be parallel to the meander pattern. When this occurs then the next mitigating factor will be the fill factor and the absorption probability of the single nanowire film[12]. Therefore, the total probability of absorption can be expressed as the product of the fill factor and absorption probability of the single nanowire nanowire[39]. The proportion of the meander area actually covered by the nanowire is the fill factor; this is the area actually capable of absorbing photons.

The thin film is usually metallic in nature, like NbTiN, and is reflective in nature. As a result the probability of absorption of a single nanowire is much less than one.

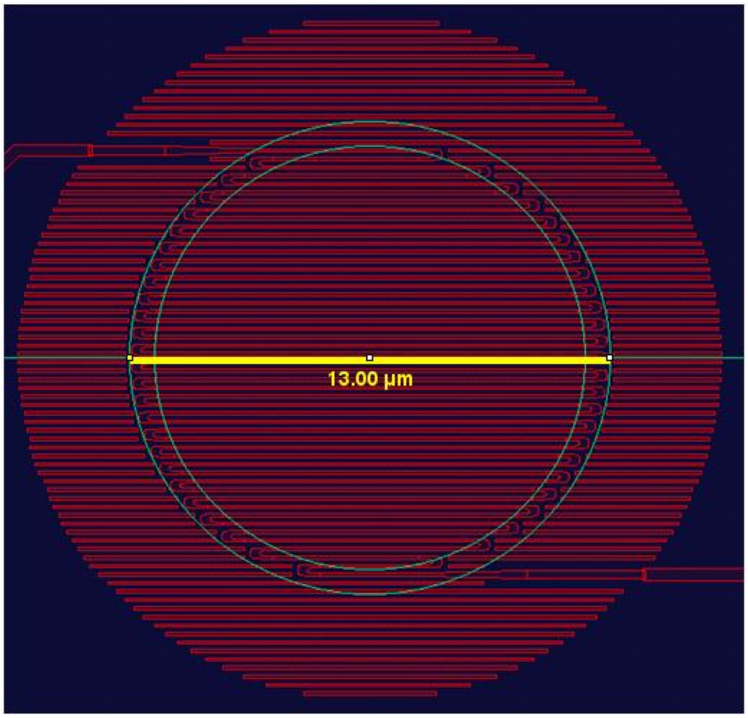

Figure 2-4: Drawing of NbTiN SNSPD meander with 180^{o} bends and active area diameter of 13µm

2.1.6 Internal and external sources of dark count

Dark counts that originate internally are due to intrinsic properties of the device and cannot be removed easily. These dark counts are accentuated as the bias current approaches the critical current of the device. Experimental results also show that these dark counts have similar voltage response profiles as a pulse from a photon count. Therefore, the hotspot size resistivity barrier created by the dark count is similar to that created by photon absorption. It is also shown in experiment that the dark count varies in a similar nature with bias current to detection efficiency and bias current. Hence, there is a similarity between the mechanism behind dark counts and photon detection. The mechanism for dark counts found in most SNSPDs is local resistance fluctuations that result in fleeting resistive states in the SNSPD when it is biased near the critical current and accentuated by joule heating during the same electro-thermal process found in the photo response after photon absorption[14],[40],[41],[42].

Externally initiated dark counts can be attributed to electrical noise from the readout circuits or the absorption of stray photons not meant to be directed at the nanowire. The electrical noise can be attributed to electrical reflections due to impedance mismatches in the transmission line, fluctuations in the DC bias current or the coupling of Nyquist noise through the readout electronics at room temperature[1]. Moreover, any stray photons may be as a result of photons from the surrounding coupling into fiber optic channel serving as the main source of photons meant to be delivered to the superconducting nanowire or they may originate from blackbody radiation. However, blackbody radiation from an emitter at 4.2 K (liquid helium temperatures), emits few visible or near infrared photons. Only these photons are of concern because the SNSPD is not sensitive to mid infrared or longer wavelengths[1]. Therefore, through proper packaging design and dark measurements at very low temperatures, these external factors can be mitigated.

2.1.7 Sources of timing jitter

As described previously, timing jitter is the uncertainty in the delay between when the photon is absorbed and when the device responds with an electrical pulse. In applications such as QKD, the time stamping interval of photon arrival is determined by total system jitter. Thus, in matching the source rate with the localization resolution of the time stamper we find that total jitter in effect reduces our pair production rate at the source.

There are two main sources of timing jitter. The first is intrinsic timing jitter. Intrinsic timing jitter is due to the dynamic nature of the photon absorption and resistive barrier formation process. The key to mitigating this source of timing jitter starts in the fabrication process where a thicker thin film can lead to better uniformity both in epitaxial growing and electron beam lithography. This will lead to less time variation in the dynamic photo response.

The external sources of timing jitter are noise and other variations within the readout electronics and dispersion in fiber optic cable over large distances. Noise induced jitter may be accentuated by the kinetic inductance of the superconducting nanowire. The fast dynamic photo response process involved in resistive barrier formation and collapse in time is affected by the material, geometry, and charge time of the nanowire. The kinetic inductance plays a key role in the charge time the larger the kinetic inductance the slower the electrical charge time. Meanwhile, chromatic dispersion in SMF fiber optic cable over long distances contributes externally to timing jitter. This is due to spread in arrival times of different wavelengths. This time spread, Δt , can be expressed as;

$$\Delta \boldsymbol{t}_{\boldsymbol{CD}} = \boldsymbol{D}_{\boldsymbol{CD}} \boldsymbol{L} \Delta \boldsymbol{\lambda} \qquad (\mathbf{2.25})$$

Where D_{CD} is the chromatic dispersion coefficient, L , is the length of the fiber, and $\Delta\lambda$ is the width of the spectrum of the laser source. At the 1550 nm wavelength, $D_{CD} < 20\, ps/(km\, nm)$. In addition, timing jitter can be introduced by polarization mode dispersion (PMD) in SMF fiber. The two orthogonal principle states of polarization can experience dispersion causing them to travel at different speeds due to geometrical and mechanical asymmetry and lack of homogeneity in the SMF fiber core. This timing jitter takes a Gaussian distribution as well, and the RMS value of the jitter, Δt_{PMD} , is expressed as

$$\Delta \boldsymbol{t}_{\boldsymbol{PMD}} = \boldsymbol{D}_{\boldsymbol{PMD}}\sqrt{\boldsymbol{L}} \quad (\mathbf{2.26})$$

Where L is the fiber length and D_{PMD} is the PMD coefficient. This coefficient is typically less than $0.5\, ps/\sqrt{km}$ [43].

2.2 Electrical device model

2.2.1 Electrical model for a SNSPD with a single un-patterned nanowire

Figure 2-5, represents the equivalent circuit of the SNSPD to account for the photo responses that occur when a photon of energy hv is incident and absorbed to create a resistive hot spot. Here the magnetic inductance of the nanowire is assumed to be negligible compared to the kinetic inductance. In addition, when there is not hotspot formation the switch is closed. As a result, the SNSPD shows zero resistance (R_{SNSPD} =0 Ω) and is in full superconducting mode as the transmission line impedance resistor is shunted. The 50 Ω impendence represents that of the transmission line and read out instruments. When a photon is absorbed and a resultant resistive barrier is created, the switch is opened and the bias current experiences a resistance, $R_{SNSPD} \gg 50\, \Omega$ due to this resistive barrier; at this point the critical current is less than the bias current. As a result, the bias current is shunted into the 50Ω impedance. This is done within a time period known as the rise time. The hotspot formation is simulated by opening the switch and closing it again on a time scale of 10 s of picoseconds. A voltage pulse $V_R(t)$ due to the resistive barrier flows through the 50 Ω impendence transmission line and read out instruments. When the hotspot resides the bias current returns to the SNSPD within a minimum time period known as the fall time.

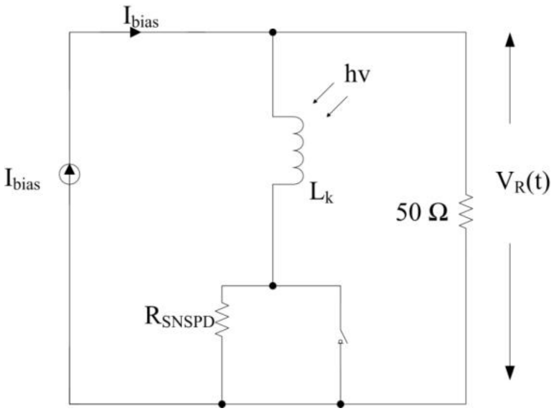

Figure 2-5: Circuit model to account for the SNSPD photoresponse when an incident photon of energy hv is absorbed by a superconducting nanowire of kinetic inductance, L_k, the voltage response , $V_R(t)$, is along the transmission line of impedance, 50 Ω

The rise time of the SNSPD voltage response due to a hotspot formation τ_1 can be expressed as the ratio of the kinetic impedance and resistance due to the resistive barrier and transmission line impedance. Here L_k is the kinetic inductance of the nanowire at zero bias current. approximate fall time, τ_2 of the SNSPD can be expressed as the ratio of the nanowire kinetic inductance and transmission line impendence because the resistance due to the SNSPD is much less than 50Ω at this point.[26].

$$\textbf{Rise time,}\boldsymbol{\tau_1 = \frac{L_k}{50 + R_{SNSPD}}} \qquad \mathbf{(2.27)}$$

$$\textbf{Fall time, }\boldsymbol{\tau_2 = \frac{L_k}{50}} \qquad \mathbf{(2.28)}$$

$$\textbf{Dead time, }\boldsymbol{\tau = \tau_1 + \tau_2 \approx \tau_2} \qquad \mathbf{(2.29)}$$

2.2.2 SNSPD experimental voltage response

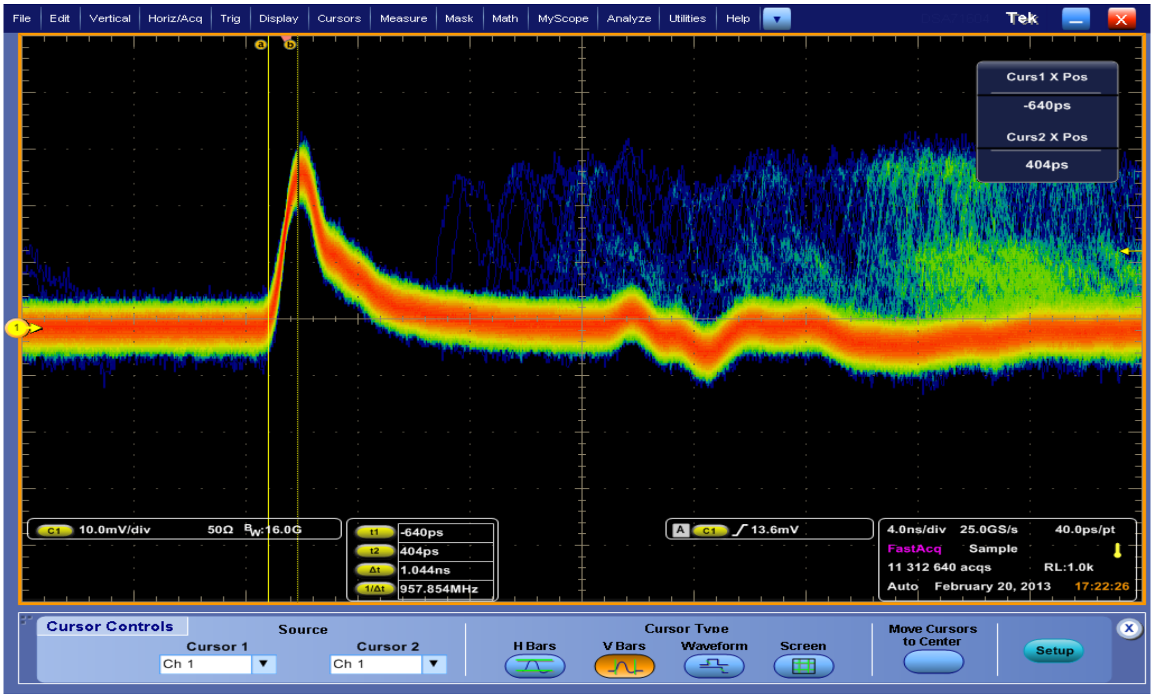

Curs1 X Pos
-640ps
Curs2 X Pos
404ps

C1 10.0mV/div 50Ω BW:16.0G

t1 -640ps
t2 404ps
Δt 1.044ns
1/Δt 957.854MHz

A C1 13.6mV

4.0ns/div 25.0GS/s 40.0ps/pt
FastAcq Sample
11 312 640 acqs RL:1.0k
Auto February 20, 2013 17:22:26

Source
Cursor 1: Ch 1
Cursor 2: Ch 1
Cursor Type

Figure 2-6: The actual NbTiN superconducting nanowire voltage response with rise time in the range of 350-400ps and recovery time is 10.24ns.

Figure 2-6 shows the actual voltage response of a NbTiN thin film single nanowire with a 180^{o} bend of approximately ~5 µm in length on either side of the bend with spacing of 300 nm, 100 nm in width, and 8 nm in thicknesss. The bend is optimal for the creation of efficient meanders with low dark count as will be elaborated on in section 2.3.1. The precise value of the hotspot resistance, R_{SNSPD} , and recovery time is difficult to precisely acquire from this voltage response plot. The rise time can be estimated to be in the region of 350 ps to 400 ps. The recovery time can be more accurately approximated as 4 times the fall time constant in this case i.e.$4\tau_2 \approx 10.24\, ns$. $4\tau_2$ is the time required for 98% of the bias current that has been shunted into 50Ω transmission line load to return into the SNSPD. This is process is known as self-resting. This self-reset occurs as long as the recovery time of the SNSPD is greater than the time it takes to cool the hotpot formation. Therefore, τ_2 can also be thought as being the minimum recovery time for the SNSPD to self-reset. Latching, previously mention in section 2.1.5, occurs when τ_2 is too small for the self-rest to occur.

The fall time is estimated to be 2.56 ns. This implies that the kinectic inductance plus the total inductance in series with the nanowire is approximately 128 nH when the inductance on the printed circuit board connecting the nanowire to the transmission line and that of the transmission line itself is considered. The accurate values for the hotspot resistance can be found by simulating the actual voltage response with the same time profile. Note that we expect the kinetic inductance of the nanowire to be in the range of $\geq 300\ pH$.

2.2.3 SPICE simulations

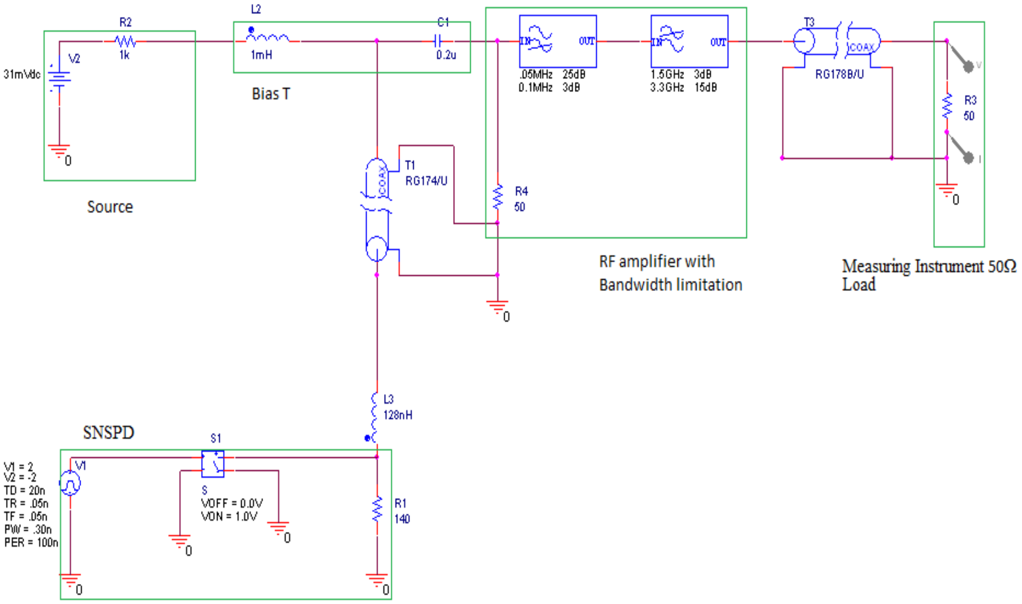

Figure 2-7: The SPICE model used to simulate the SNSPD response. The various components used include the current source, bias tee, RF amplifier, SNSPD, RF coaxial cables.

Figure 2-7, shows the overall SNSPD schematic used to model the photo response. The model is similar to the one used by Orgiazzi[4]. A current source, modeled as a voltage source is feed into a Bias T. The Bias T has an inductance and capacitance that were previously known. The Bias T is connected to a RF amplifier and a SPICE model for a microwave cable. The input impedance and bandwidth limitation of the amplifier is taken in to account; however, the gain of the amplifier is neglected for this simulation. The amplifier has a low pass filter in series with a high pass filter. The R_4 resistor represents the total resistance seen by the rest of the circuit from the SNSPD during the photo response process. The current passing through R_4 is due to the pulse controlled switch that is SET ON during the photo response, which creates a picoseconds voltage pulse. The total inductance value calculated based on experimental results highlighted in figure 2-6. A value for R_4

was estimated until the simulated response had a total deadtime period and response profile equivalent to that of figure 2-6. Not surprisingly, the R_4 value matched that of the gradient of the IV curve for the superconducting nanowire found during experiment. However, it must be noted that this value of R_4 includes not just that of the resistive barrier formed during the photo response process, but also the value of the resistance of the gold pad on the chip substrate used to form the electrical connections to the superconducting nanowire; this resistance is in series with the resistive barrier.

Figure 2-8 and figure 2-6 show a similarity in the minute dip created in the response profile just after the peak. This minute dip that occurs after the fast rise time of the voltage pulse is due to the limited bandwidth of the RF amplifier, which is around 1.5 Ghz. A portion of the high frequency components of the voltage pulse is reflected back to the SNSPD after traversing twice the length of the transmission line because below 900 MHz, the voltage standing wave ratio VSWR is less than 2 [4].

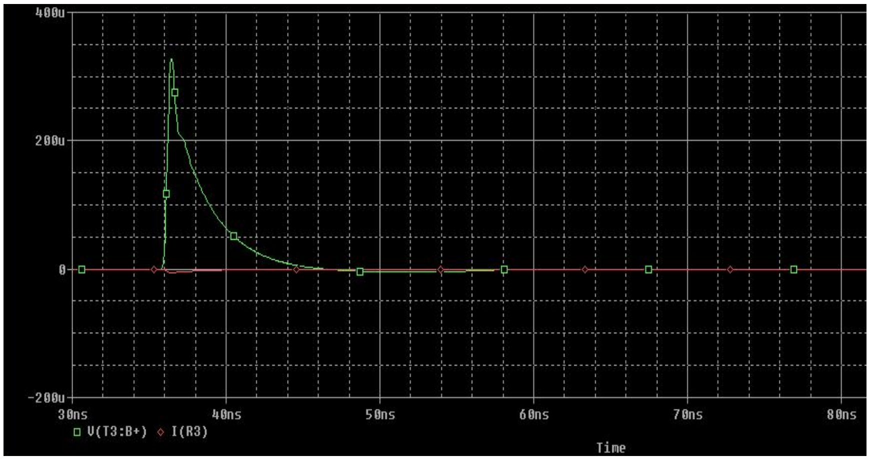

Figure 2-8: Spice simulation of the voltage pulse due to the photo response process for the electrical circuit simulation. (Green curve is voltage, red curve is current across the 50 Ω load)

Moreover, when the non-ideal input impendence of the RF amplifier is taken into consideration, a dip is seen in the profile of figure 2-9 at 14 ns after the voltage pulse peak. This mirrors exactly what is seen in figure 2-6. In summary, the SNSPD series inductance and SNSPD resistance during the photo response process is confirmed to be 128 nH and 140 Ω.

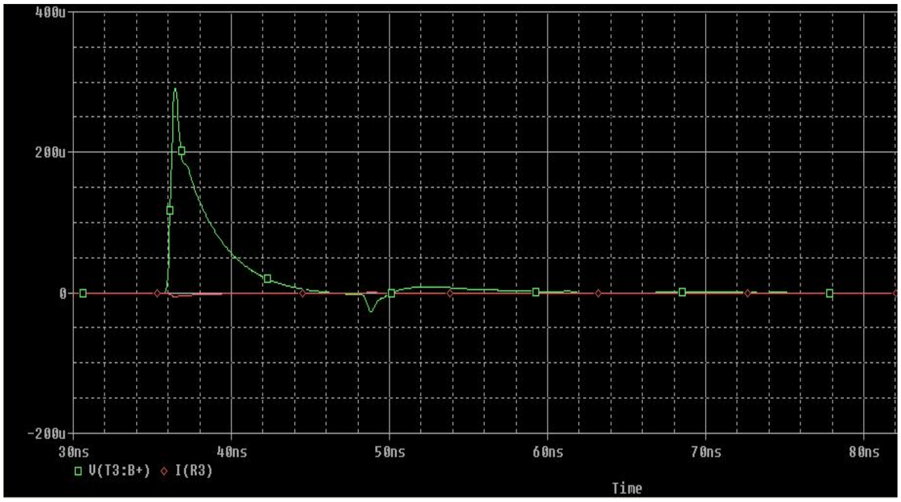

Figure 2-9: Spice simulation of the voltage pulse due to the photo response process for the electrical circuit simulation after the non-ideal input impedance of the amplifier was considered and R_4 was set to 40 Ω

2.3 Device Fabrication

2.3.1 Device Schematics

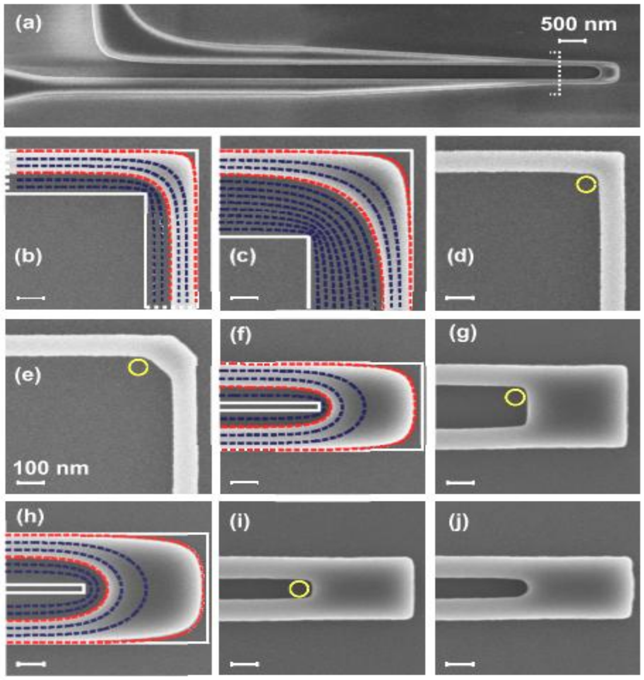

Figure 2-10: SEM images of nanowires with different degree's of bending explored by Akhlaghi et . al.[44] **(a) A typical nanowire structure (b) and (c) two optimized 90^0 bends. (d) and (e) sharp 45^0 and 90^0 bends. (f) and (g) optimized and sharp 180^0 turns with 200 nm spacing. (h) optimized 180^0 turn with 300 nm spacing. (i) and (j) sharp and circular (radius = 50 nm) 180^0 turns with 100nm spacing. The circles are eye guides with 35 nm radius. Blue and red dashed lines are current streamlines calculated for a superconductor thin film enclosed by solid white lines. All the parts, except (a) share the same length scale**

Recently, Akhlaghi et al.[44] found that superconducting nanowires with varying degrees of bend and spacing have different dark count, critical current, and hence, detection efficiency values. This study is important because it sheds light on what is needed to achieve SNSPD meanders with higher overall detection efficiency and lower dark counts. Higher overall detection efficiency and lower dark count with ever present low timing jitter of the SNSPD will make such a packaged superconducting nanowire meander a prime candidate for applications, such as long distance quantum key distribution. Though SNSPD meanders are typically have 180^0 turns with (~100 nm wide nanowires), these bends are usually placed outside the photon absorbing area and do not contribute to photon detection. However, current crowding at these sharp turns has the effect of reducing the measured critical current of the superconducting nanowire meander. The effects of suboptimal bending on dark count and critical current are explored on the device shown in figure 2-11. The device is fabricated on a SiO_2 substrate with 8 nm thick NbTiN thin film. Despite having different bends, the wires all share the same dimensions and superconducting thin film quality, within their respective active areas. This mitigates the slight width changes when different geometries are exposed by the electron beam and effects due to resist variation and proximity dose effects, etc. Of all the various bends shown in figure 2-10, the 180^0 bend with a big enough footprint to support the optimized meander design (white circle in figure 2-11) shows dark count levels at higher bias currents, detection efficiency at higher bias currents. The sharpness of the bends is proportional to the current crowding observed. Note that in fabricating a SNSPD meander with the optimal 180^0 bends, care must be taken not to produce any sharp bends in the process or the overall performance of the superconducting meander will suffer.

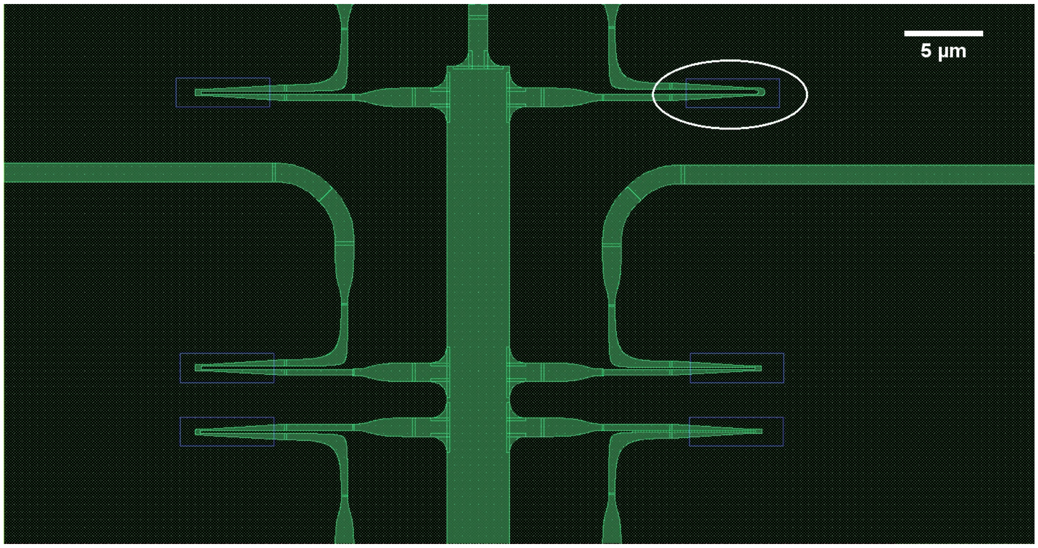

Figure 2-11: Drawing of the actual device containing the nanowires of varying bends shown in figure 2-10. The wire with the most optimal bending profile is en-cirlced; the inner blue square represents the active area of the nanowire. This wire was tested using the packaging and cryogenic probe whose design is the focal point of this master's thesis.

2.3.2 Brief overview of Fabrication steps for the NBTiN nanowire structure on oxidized silicon and its inherent advantages

With the use of ion beam milling with Argon gas, the nanowire configuration seen in figure 2-11 are transferred into the NbTiN thin film. But first a Hydrogen silsesquioxane resist is first developed in a tetra-methyl ammonium hydroxide solution. Next, the Hydrogen silsesquioxane resist is spin-coated, then patterned using 125 KeV electron-beam lithography. During the fabrication process, the write parameters are painstakingly tuned so that the nanostructures are as similar as possible and within the confines of the designed curvatures as outlined with the red dashed lines on figure 2-10. Despite the fact that 8 nm of thin film thickness was deposited, the effective superconducting thickness is expected to be smaller because of surface effects. The measured critical temperature after nano-patterning was approximately 8.4 K[44].

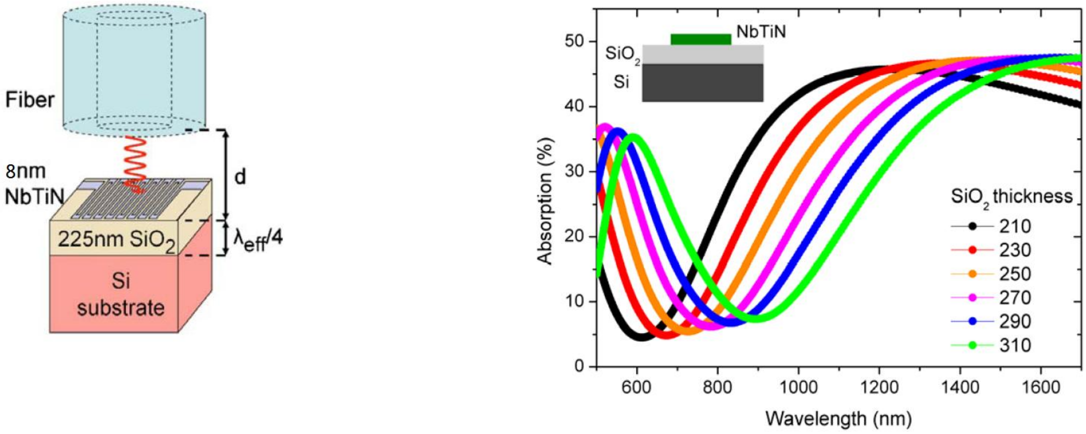

Figure 2-12: (Left) Oxidized silicon substrate composition for final tuned etch of chip substrate used for the nanowire bends seen in figure 2-11. The effective wave length λ_{eff} is a function of photon wavelength and the refractive index of SiO_2.The figure depicts the alignment of a SMF-28e fiber core with an 8nm thick NbTiN nanowire. (Right) Absorption of photons at different SiO_2 thickness levels [15],[45]**.**

While the substrate for the structure shown in figure 2-11 is optimized for the 1310 nm telecom wavelength. In the work done by Tanner et al.[15], we see increased absorption for the nanowire compared to that of the NbN SNSPD for a 6 nm thick NbTiN layer of thin film using a continuous wave laser diode source [23]. For photons of wavelength, $\lambda = 4n_{SiO2}\Delta d$ we see this enhancement. Where, n_{SiO2}, is the refractive index of the SiO_2 layer ~1.45 and Δd is the thickness of the SiO_2 layer[15]. Cavity like behavior is observed as extra reflections occur at the SiO_2/Si boundary resulting in constructive interference at the chip surface. Peak absorption of photons occurred at the 1310 nm telecom wavelength exhibiting a value of ~65% absorption. While the cavity was not optimized for 1550 nm, increased detection efficiency is still observed at this wavelength. For optimal absorption at 1550nm, Δd, will have to be made larger. The variation of absorption with Δd at 1550nm is seen in figure 2-12.

Chapter 3

Experimentation and preparation of system for potential QKD implementation

3.1 Cryogenic equipment

Any cryogenic setup designed for the efficient and continuous use of the SNSPD in different applications, like characterization of an SNSPD or quantum key distribution (QKD) needs to meet a minimum set of requirements. Firstly, implementation of the packaged SNSPD can be over a time span of a few hours to several days; therefore, the packaging and cryogenic design should consume helium economically. Secondly, efficient shielding from background electromagnetic radiation and stray light should be provided so as to minimize the dark count due to external factors. Thirdly, the SNSPD packaging should provide good thermal conduction for the SNSPD to maintain stable operating temperatures of around 4 K. Finally, the packaging should be structurally sound and able to withstand thermal contractions while maintaining the integrity of any results yielded every time it is used[4].

The first overarching detail that touches on all the requirements listed above is the choice of material for the cryogenic packaging and dipper probe. Several options were explored, but in the end Invar 36 for the packaging, copper for base of the dipper probe, and stainless steel 304 for the rest of the dipper probe were chosen. The choice of invar 36 was based on the thermal expansion properties of invar and its match to that of the SNSPD substrate and it's resilience to thermal contraction that will facilitate alignment of the 9 µm wide SMF-28 fiber core to a 10-13 µm SNSPD meander active area diameter or 100 nm wide single nanowire with a bend. In addition, Invar 36 experiences a low temperature fluctuations and a steady rate of contraction while cooling down to 4.2 K. Figure 3-1, highlights this fact. Indeed, between 294 K and 4 K the total linear expansion coefficient is 0.04% and the thermal conduction of 0.24 W/(m.K), which is much lower than copper but this deficiency is heavily offset by it's more important thermal expansion properties. Note that between 294 K and 4 K the total linear expansion coefficient for copper is 0.324% and that of silicon is 0.022%. Moreover, because of its high thermal conduction copper was chosen as the main interface between the packaging that outer dipper probe. This will facilitate good conduction of heat away from the packaging and into the liquid helium environment. Stainless steel was an easy choice for the dipper probe because its sturdiness and low thermal conduction of 0.27 W/(m.K) means less transfer of heat from the surrounding into the liquid helium bath leading to the unnecessary wasting of helium[46].

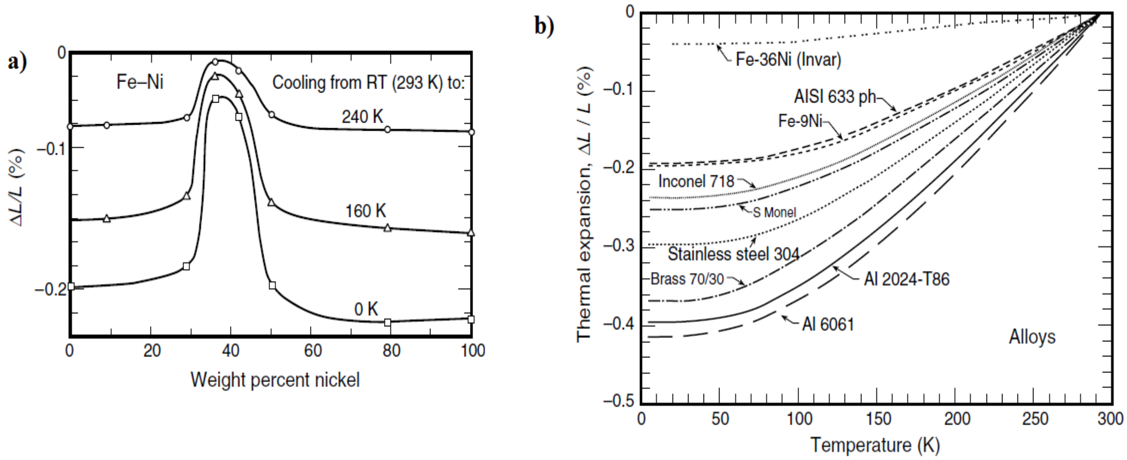

Figure 3-1: a) shows the thermal expansion from room temperature to 0 K. The steady contraction of Invar 36 (Fe-Ni), which comprises of 36% nickel is seen; b) Compares the thermal linear contraction of common alloys[4][46]**.**

3.1.1 Packaging design and fabrication

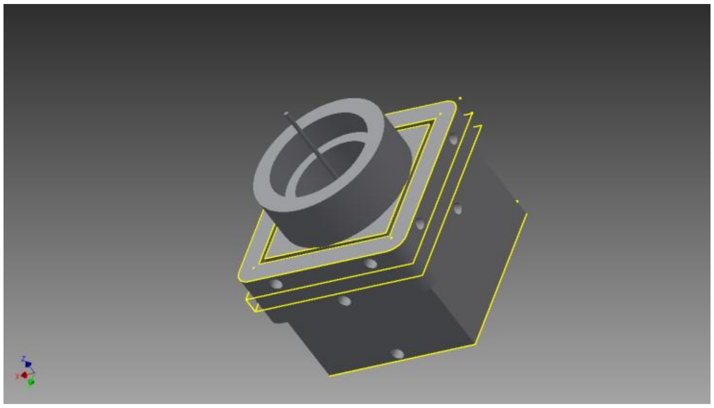

Figure 3-2: 3-dimensional CAD drawing of the packaging

Figure 3-2 above shows a 3-dimensional depiction of the invar 36 packaging that was designed and fabricated. The dimensions are approximately 23 mm in height and 23 mm in length and breadth at its widest points. The different parts that comprise the packaging are shown in figure 3-3 below. The main body, mounting plate, cover, locking rings and adjustment screws are all made of invar 36. The outer dimensions of the packaging body are 20 mm x 20 mm x 12.7 mm. The cover overlaps the body and has outer dimensions of 23 mm x 23 mm x 7 mm and features an inner horizontal adjustment plate that allows 50 µm incremental adjustments in the x-y plane of the fiber ferrule. A pigtailed ferrule connected to a SMF 28 fiber is used as the main channel for photons into the packaging. The ferrule is 5.5 mm in length and 1.8 mm in diameter with anti-reflection coating (Thorlabs part number: SMPF0115). The fiber is held in place with STYCAST ® 2850 FT epoxy in a custom made ½-80 vertical adjustment screw capable of 317.5 µm adjustments of the fiber ferrule tip per turn of the screw. An outer locking ring is used to hold the screw in place once its set and inner locking ring is used lock the angular adjustment ball with stem that allows minute off center angular movement of the ferrule tip.

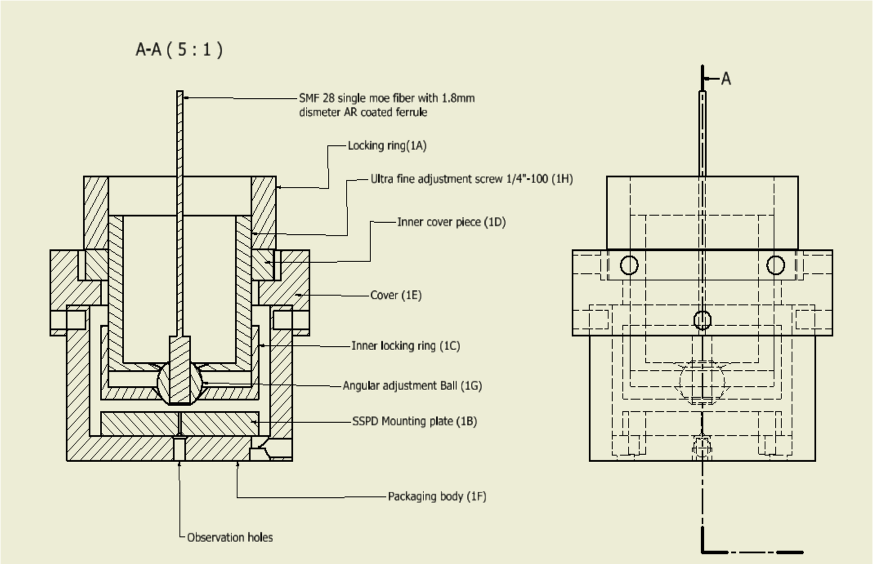

Figure 3-3: Front and cross sectional view of the CAD drawing for the packaging assembly

3.1.2 Dipper probe specifications

The dipper probe was designed with the potential application in mind i.e. characterizing superconducting nanowire devices, QKD, single photon source characterization, etc. Therefore the main aspect of the probe would be its economical use of liquid helium. One way to do this is to design a probe that inserts directly into a Dewar of liquid helium; the Dewar then effectively acts as a cryostat. Besides the packaging, the 1/2" stainless steel probe with 0.9 mm wall thickness, contains 4 lengths of manganin wire, one length of coaxial cable, one length of SMF 28e optical fiber with 900 µm jacket.

Helium consumption was estimated by looking at the total heat transfer into the Dewar, q_{in} ,by the dipper probe through the stainless steel tube, q_{steel} , the 4 lengths of manganin wire, q_{mag} , one length of coaxial cable, q_{coax}, one length of SMF 28e optical fiber, q_{fiber}, with 900 µm jacket[46]. The coax cable is a special case in that, $q_{coax} = q_{sheild} + q_{core} + q_{dielectirc}$, where the core is 150 µm thick copper wires, the shield is fifty 100 µm diameter in a braid, and the dielectric is 2 mm thick.

Let the heat transferred into the Dewar by the latter mentioned components can be described as:

$$\boldsymbol{q_{in} = q_{steel} + q_{mag} + q_{coax} + q_{fiber}} \qquad (\mathbf{3.1})$$

Liquid helium has a boiling point of 4.2 K at one atmosphere and a latent heat of evaporation of 2.6 kJ/L. For a 60 L Dewar of liquid this means 1.4 L/Wh. Therefore, q_{in} by no means represents the main source of liquid helium consumption. Neglecting the heat contribution of the optical fiber we arrive at a value for dipper probe helium consumption listed in reference[46]:

Heat transfer due to stainless steel, $q_{steel} = \frac{A}{L}\int_{4K}^{300K} \lambda(T)dT$

Heat transfer due to 300µm thick Manganin wires, $q_{mag} = 4 \times \frac{A}{L}\int_{4K}^{300K} \lambda(T)dT$

Heat transfer due to single RG174 coax cable, $q_{coax} = \frac{A_1}{L}\int_{4K}^{300K} \lambda_1(T)dT + \frac{A_2}{L}\int_{4K}^{300K} \lambda_2(T)dT + \frac{A_2}{L}\int_{4K}^{300K} \lambda_2(T)dT$

Using the values given in the latter mentioned reference we arrive at:

$$q_{steel} = \pi(0.0127)(0.001016)(0.88)(3.06 \times 1000)W \approx 140\,mW$$

$$q_{mag} = 4\pi(0.000150)^2(1)(5.16)(1000) \approx 1.46\text{mW}$$

$$q_{coax} \approx 53mW + 16.7mW + 1.3mW \approx 71\,mW$$

Therefore, Total heat input, $q_{in} \approx 212.46\,mW$. This implies a consumption rate of approximately 3 liters per day. This result assumes that the boil-of gas does not efficiently cool a significant length of the tube not directly inserted in liquid helium. Thus cooling effect due to the latter is assumed negligible.

The dipper probe assembly comprises of an upper compartment, a stainless steel rod, and a lower compartment, as shown in figure 3-4 & 3-5. The upper compartment contains two pairs of FC/PC and SMA ports facilitating the ability to connect two SNSPD devices in parallel if needed. It also contains a 1/3 psi vent relief valve that releases the sudden build up in internal pressure as the helium gas within expands upon removal of the probe from the Dewar. The top compartment also features a hermetically sealed fischer connector that connects to 2 pairs of twisted wires that connect the thermal sensor. The top compartment is sealed with an o ring fitting.

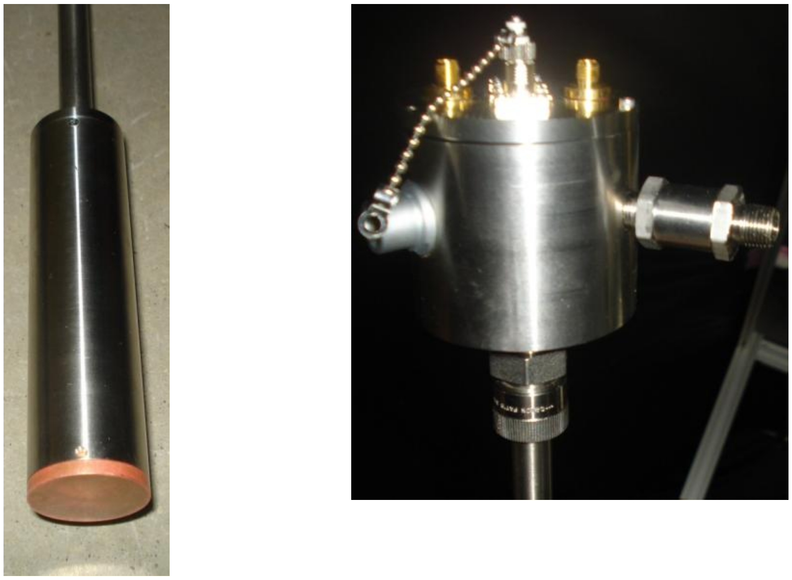

Figure 3-4: Picture of top of dipper probe featuring a 1/3 psi vent belief valve, fischer hermatic connector for temperature readout instruments, FC/PC mating connector, and SMA connectors (Right). Dipper probe compartment that contains the SNSPD device, thermal senor, and packaging with copper base (left).

A single coaxial cable, 2 pairs of twisted wire, and a single length of SMF-28e fiber optic cable run the length of the stainless steel rod that connects the lower compartment. Along the length of the rod we placed an adjustable flange that allows the lower compartment to be placed at different controlled depths into the liquid helium Dewar. The lower compartment contains the packaging and connects to the coaxial cable, the fiber optic cable, and is fitted with the thermal sensor to monitor the packaging and SNSPD operating temperature

Figure 3-5: Top view of entire dipper probe

3.2 Optical apparatus

3.2.1 Pulsed Laser characterization

In this section we explore the characterization of short pulsed laser source that can be used to test the functionality of our packaging and SNSPD meander device. The laser is designed by ID Quantique (id-300-1550-DFB-TTL 50 Ω)[47]. The product manufacturer specifies a peak power of 1 mW and pulse duration at FWHM of 300 ps, shown in figure 3-6. Given that the average power of the laser at 1MHz is -35 dBm, we proceed to calculate the pulse energy and mean photons per pulse. In practice, one will attenuate the laser until the average number of photons per pulse is equivalent to 0.1 photons per pulse. This is the case because Poisson distribution of the photon arrivals described below in equation 3.5. The probability of a single photon arrival is maximized when the average photon number is much less than one. Our findings show that this occurs at approximately -73 dB. Of course, in the actual implementation, the spot size incident on the SNSPD active area must also be considered in estimating an appropriate attenuation level.

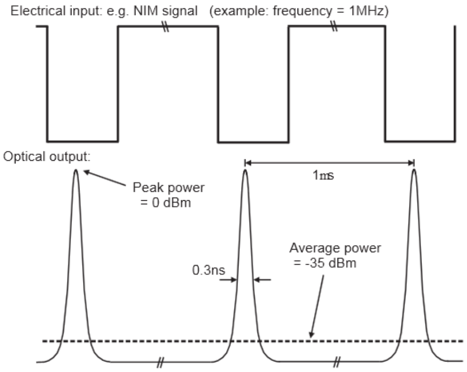

Figure 3-6: Pulsed laser frequency profile at a trigger rate of 1MHz[47]

Power at 1MHz, $P_{1MHz} = -35\text{dBm} = 10^{-3.5}$ mW

Let, the energy per pulse, $E_P = \frac{P_{1MHz}}{10^6} = 10^{-9.5}\ mJ$

Quantum mechanics stipulates that, energy of a single photon, $E_\lambda = \frac{hc}{\lambda}$. This relation coupled with the latter calculation and the experimental data we collected led to figure 3-7, where we compare the experimental power output to the theoretical output for different frequencies of interest. Note that a Tektronix function generator, EXFO variable attenuator, and Oz Optics power (POM-300) meter were used.

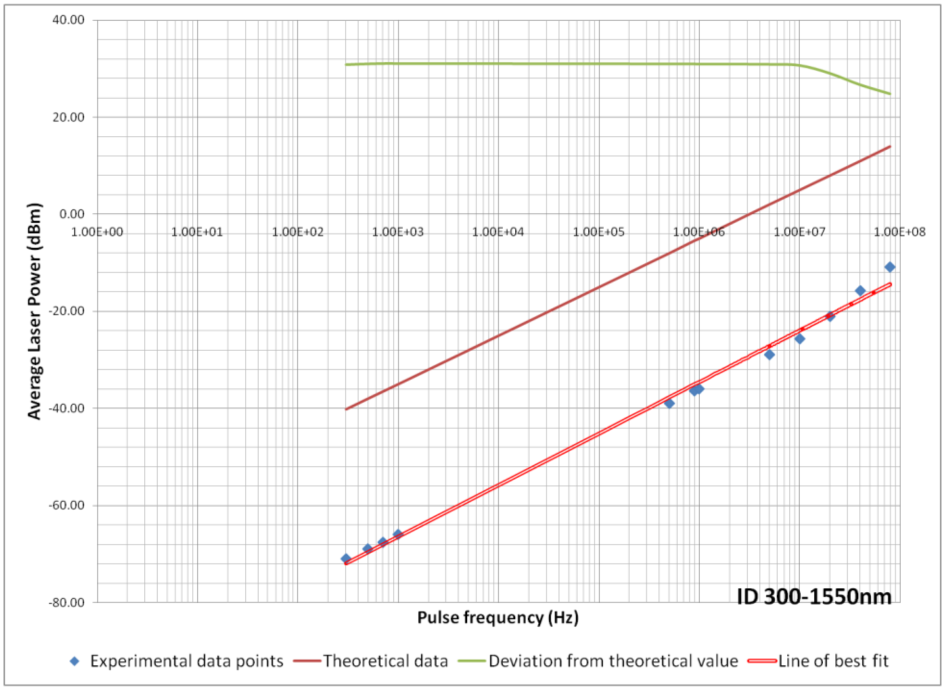

Figure 3-7: Experimental power and theoretical power in dBm for a 1550 nm ID 300 pulsed laser from ID-Quantique

Up to 10 MHz triggered output by the laser, a constant experimental vs theoretical power output difference of approximately 0.89 dB is observed. This is a combination of loss in the connectors and manufacturer specified precision$\pm 1\ dB$. After 10 MHz output the laser output begins to approach its theoretical value at higher power output levels.

For this characterizing a SNSPD meander, we are interested in a laser source frequency of 1 MHz or greater. This pulsed source is assumed to be coherent according to manufacturer specifications. At 1 MHz the average number of photons per pulse at the 1550 nm wavelength can be found as;

$$\text{Un-attenuated average photon per pulse at 1MHz, } \overline{N_1} \approx \frac{E_P}{E_\lambda} = 2.45 \times 10^6$$

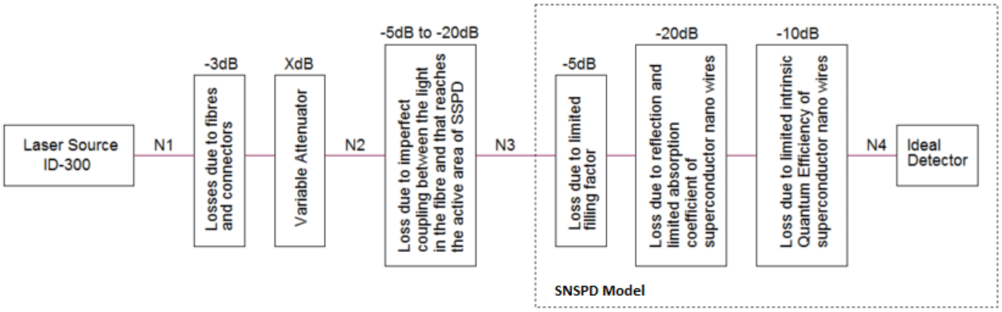

Figure 3-8: Attenuation model used by Orgiazzi [4] **under a similar set of circumstances. The attenuation levels used for the SNSPD model are only estimates but are satisfactory for our purposes.**

We can now use the model highlighted in figure 3-8 to determine system quantum efficiency and detector/quantum efficiency. Where;

$$\boldsymbol{System\ quantum\ efficiency, \eta_{SQE} = \frac{\overline{N_4}}{\overline{N_2}}} \qquad (\mathbf{3.2})$$

$$\boldsymbol{Detector\ efficiency, \eta_{DE} = \frac{\overline{N_4}}{\overline{N_3}}} \qquad (\mathbf{3.3})$$

The coherent source has a constant optical power. However, the actual times of registration of a photon varies statistically. The photon arrival distribution is shown to vary as a Poisson distribution[48]. Where;

$$\textbf{Probability distribution, } \boldsymbol{p(n) = \frac{\bar{n}^n \exp(-\bar{n})}{n!}, n = 0, 1, 2, 3, \ldots} \qquad (\mathbf{3.4})$$

$p(n)$ represents the probability of getting n successes when the average number of successes is $\bar{n}$. This model can be used to design a probability of detection model for a detector that cannot distinguish the number of photons in each arriving pulse, i.e. a bucket detector. Where the probability of detection is given as;

$$\boldsymbol{P_D = 1 - \exp(-\eta_D \cdot \mu)} \qquad (\mathbf{3.5})$$

Where η_D represent the detector efficiency and μ represent the average photon number per pulse. Figure 3-9 shows experimental justification for this model. The ID Quantique ID 201 APD single photon detector and pulsed laser source ID-300 at 1550 nm is used to produce figure 3-9.

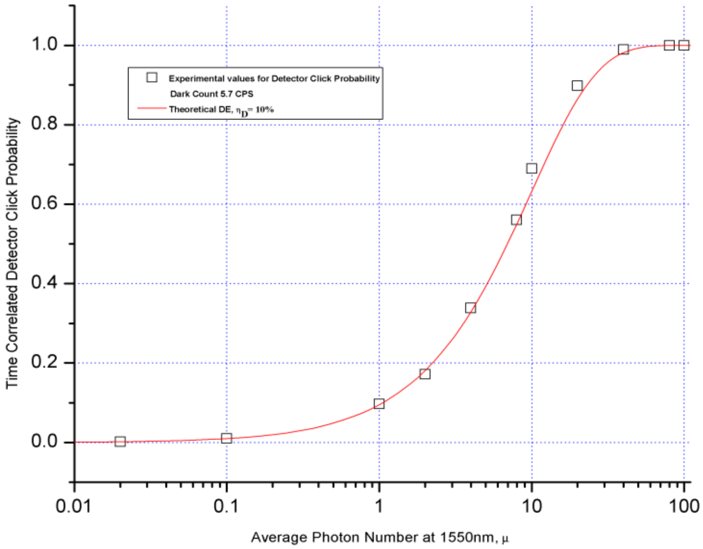

Figure 3-9: Assuming a bucket detector model, an ID Quantique ID-201 single photon detector is used to characterize the ID-300 pulsed laser source at 1550 nm. The result verifies the Poisson distribution of actual photon arrivals in a coherent pulsed laser source. A theoretical probability trend line for poisson process of photon arrivals as a function of the detector efficiency and average photons per pulse fits the experimental data quite well.

3.2.2 Continuous wave laser characterization

For the continuous wave photon source the ILX Ligthwave laser diode controller along with a NEP japan 1550nm laser diode were characterized using the same lengths of optical fiber that were to be used in the superconducting nanowire characterization experiments. The continuous wave source also follows a Poisson distribution in terms of photon number distribution. In addition, the probability of a given inter-arrival time of photons can be viewed as decaying exponentially with time. Figure 3-10 shows the relationship between photon numbers leaving the fiber with respect to different imposed attenuation levels in the range of interest for the nanowire characterization experiments. The detector efficiency is found experimentally for a single NbTiN nanowire with optimal 180^0 bend using this source. Then, through simulation we are able to stipulate the system quantum efficiency of a SNSPD meander device made with this type of quantum nanowire.

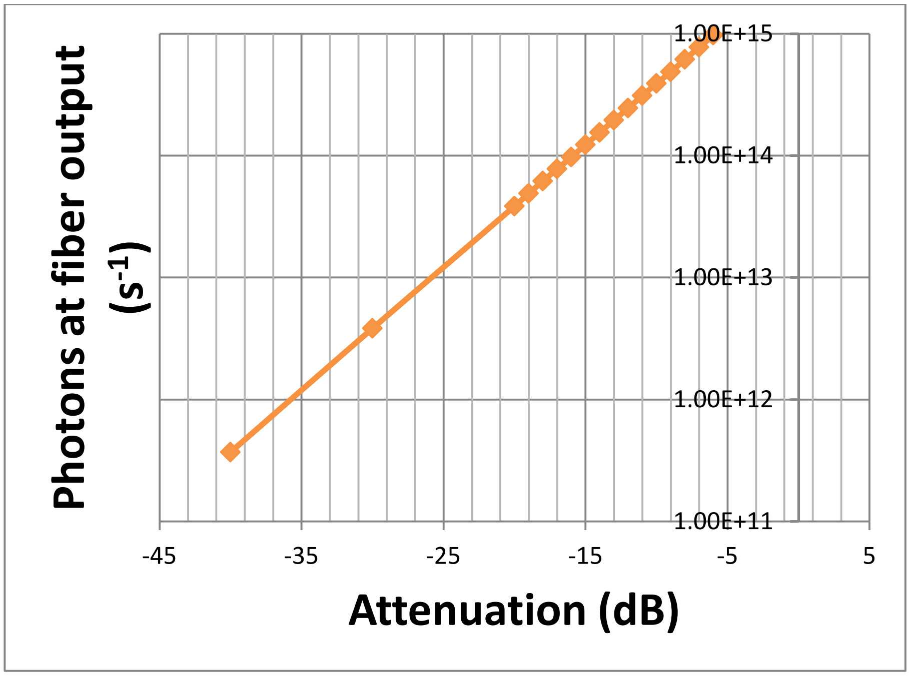

Figure 3-10: 1550 nm photon output per second at the fiber for varying levels of attenuation with the diode controller set at 100 mA current output

3.2.3 Coupling to a single un-patterned nanowire

As previously mentioned in section 2.1.5, the thin film is usually metallic in nature, like NbTiN, and is thus reflective in nature. As a result, the probability of absorption of an un-patterned nanowire is much less than one. Therefore, any attempt to directly couple a 9 µm fiber core to a 100 nm wide superconducting nanowire will result in extremely low coupling efficiency and this may not be practical in characterizing the superconducting nanowire.

The best solution is to assume an incident Gaussian beam of spot size,$\omega(z)$, at some distance z from the tip of the SMF-28e fiber ferrule. Because the wire of length, l_d has width , w_d , while the fiber core diameter, d_f , is such that $w_d \ll d_f$, we can assume uniform top surface area or the nanowire for the incident power at some distance z from the ferrule. Therefore, the fraction of power that is delivered to the surface of the 100nm thick nanowire is minuscule i.e. on the scale of $\frac{1}{100}$ of the power that leaves the fiber core within a range of 0-100 μm from the fiber tip. This fact along with a previously characterized CW laser source will give the expected number of photons arriving at the nanowire surface per second.

The mode profile in the fiber is:

$$\boldsymbol{P(r) = \frac{2}{\pi\omega_0^2} \cdot \exp\left(-\frac{2(x^2+y^2)}{\omega_0^2}\right)} \qquad (\mathbf{3.6})$$

Where ω_0 is the Gaussian beam radius.

Now, the beam radius some distance z from the fiber is given as;

$$\boldsymbol{\omega(z) = \omega_0\sqrt{1+\left(\frac{\lambda z}{\pi\omega_0^2}\right)^2}} \qquad (\mathbf{3.7})$$

And the power a distance z away is given as;

$$\boldsymbol{P(r,z) = \frac{2}{\pi\omega(z)^2} \exp\left(-\frac{2(x^2+y^2)}{w(z)^2}\right)} \qquad (\mathbf{3.8})$$

3.2.1 Optical alignment

The mounting plate of the packaging is held in place between two optical objectives. Motion of the mounting plate between these objectives is controlled by a X-Y-Z manual stage with down to 0.5 µm of precision in movement in any X, Y, or Z direction. Light from a 150W halogen lamp without any infrared filter is directed into a long-pass optical filter rated at 950 µm. This effectively sends a range of near-infrared wavelengths into an objective rated at 25x that is infrared coated. The infrared light is then focused on the observation hole at the bottom of the mounting plate. At the top of the mounting plate lies the oxidized silicon SNSPD substrate, which has been polished on both sides before fabrication. This polishing increases the oxidized silicon's transparency to near-infrared radiation.

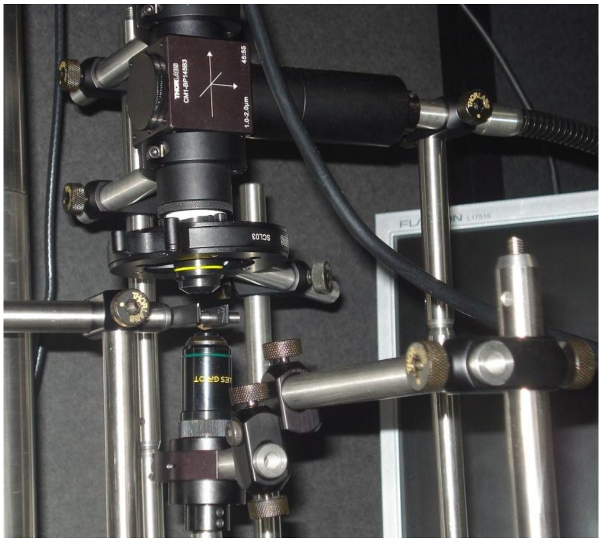

Figure 3-11: Shows 10x objective on top connected to a 50/50 beam splitter and 25x objective below used as the infrared light source for SNSPD alignment.

The second infrared coated objective at 10x located above the mounting plate is connected to a long black optical tubing, equipped with lenses to increase the focal length, and a 50/50 beam splitter that allows one to shine visible light onto the mounting plate below, making it easy to find the exact center of the SNSPD substrate where the nanowire is located. The infrared light that passes through the oxidized silicon substrate is directed into the 50/50 beam splitter through the optical tubing into a CCTV camera. The CCTV camera has been modified to record near infrared radiation and a black and white image of the SNSPD center appears on a 17” monitor. This setup allows the careful centering and adhesion of the SNSPD substrate to the exact center of the mounting plate. Once the chip is centered the ferrule is centered using the X-Y adjustment plate that is an innovative part of my packaging design. For a single nanowire the ferrule is placed the maximum distance away from the SNSPD surface for characterization. Part of the apparatus used in this alignment process is seen in figure 3-11. Figure 3-12 shows the CCTV camera image used to center the SNSPD on the mounting plate.

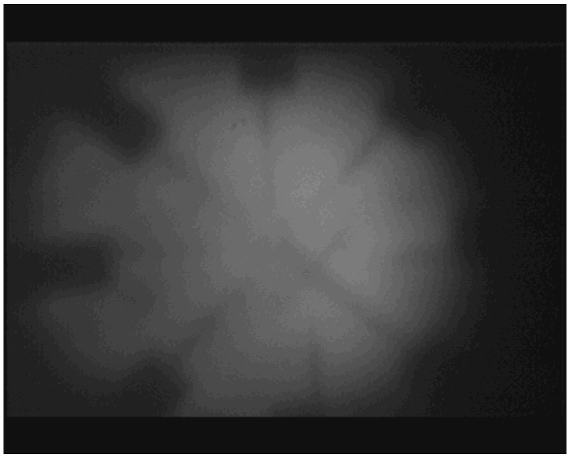

Figure 3-12: Screen capture of the center of the SNSPD. The rectangular shadows are the gold pads that connect the SNSPD. The thicker wires that lead to the nanowire structure at the center are also seen as the radial lines connected to the rectangular pads.

3.3 DC screening and measurement apparatus

3.3.1 Overview of DC screening for nanowire characterization

The first steps in characterizing the superconducting nanowire detection are ensuring that all electrical connections are working. If this is the case then a plot of temperature vs. resistance for the nanowire should be done to ensure that the packaging effectively allows the device to enter the superconducting mode. Next the SNSPD is DC current biased at various levels starting from 0A up the critical current in small steps of 1µA or less to ensure that the exact current (critical current), $I_{C,}$ that takes the wire out of the superconducting mode is recorded. The DC current source for the experiment is the keithley 2400 Broad Purpose SourceMeter. For the purposes of testing the packaging and providing information for a future SNSPD meander design the experiment is carried out at the optimal operating temperature for the superconducting nanowire i.e. 4.2 K.

3.3.2 Resistance versus temperature measurements

As previously mentioned, when a superconducting nanowire is cooled beyond it’s critical temperature,T_c, typically in the range $\frac{T_c}{2} \leq T < T_c$, DC current is able to flow through its core with zero resistance. It is this state that makes the superconducting nanowire single photon detector a possibility. Therefore, an important first step in the characterization of a single un-patterned nanowire[7] or nanowire meanders is the resistance vs. temperature measurements, as shown in figure 3-13. A hallmark of good critical current and detection efficiency of the SNSPD is a resistance vs. temperature profile that exhibits superconducting transitions at temperatures equal to or greater than the operating temperature of the device (4.2K). Otherwise, without doing further testing one can anticipate low critical current and subpar detection efficiency. The critical temperature depends most on thin film material and wire thickness. However, for wire of width less than 100 nm, width becomes an important factor in critical temperature. This is because factors such as local impurities, grain boundaries, and lattice defects become amplified for thinner wires[1]. It is important to note that resistivity per unit length of the nanowire does not strongly affect the critical temperature[1][30][16]. Figure 3-13 shows a critical temperature of approximately 10 K.

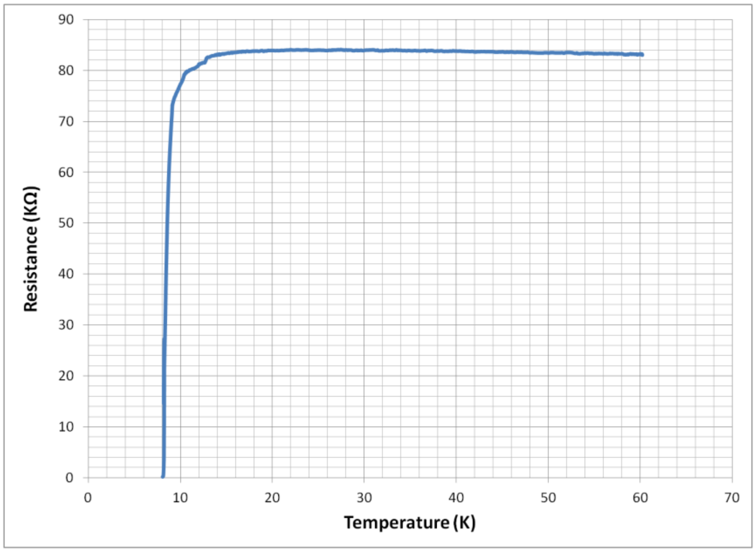

Figure 3-13: Experimental results for temperature vs. resistance for a single un-patterned NbTiN superconducting nanowire of thickness 8 nm and length of 10 µm. The minimum resistance below the critical temperature is around 130Ω due to the gold pads that connect the nanowires. This is seen more clearly in figure 3-15.

---

[7] The term un-patterned nanowire refers to the single nanowire on a substrate that does not form a complex meander with some geometrical shape with an associated filling factor.

3.3.3 Forward bias current versus voltage measurements

The critical current is our primary interest in this experiment. Once it is found that our packaging is able to exhibit a critical current for the 100 nm nanowire with optimal 180^0 bending within the range specified by Akhlaghi et al.[44], then we can proceed to making recommendations for the ideal SNSPD meander design for our SNSPD packaging.

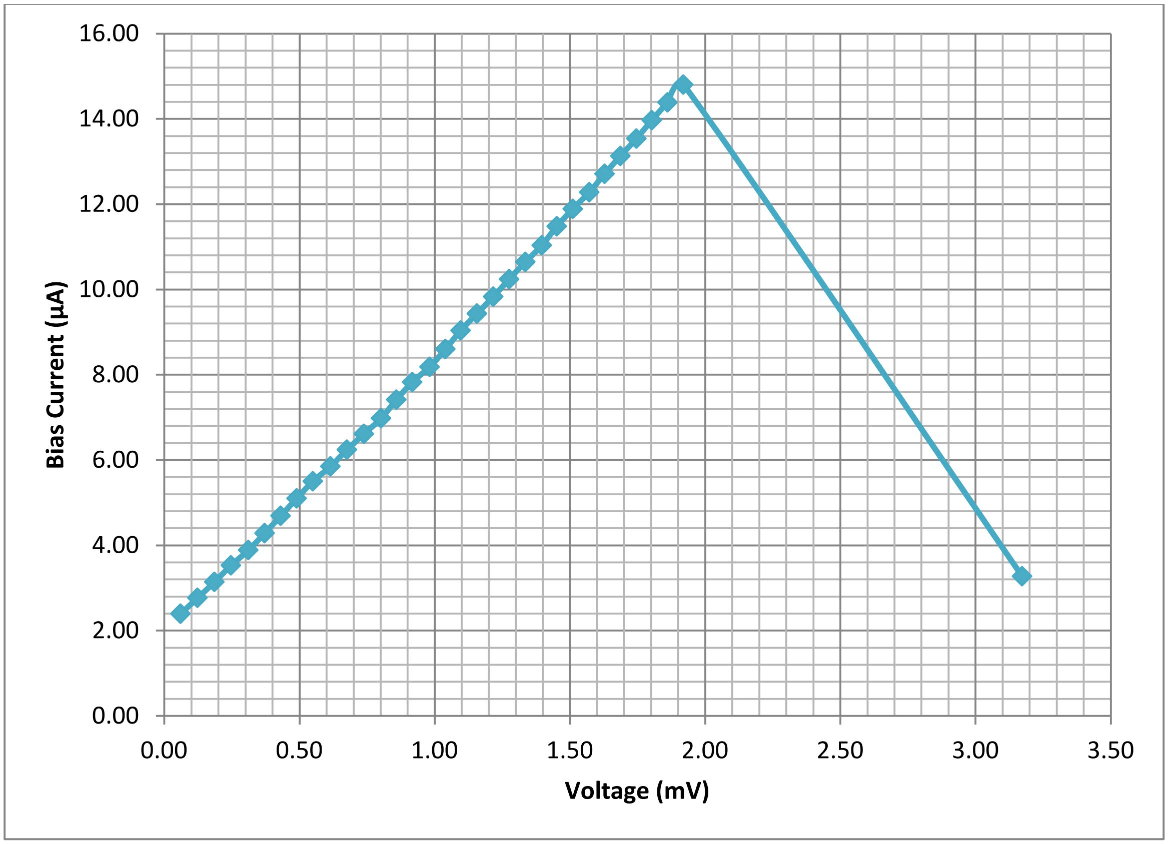

Figure 3-14: Experimental results for DC characterization of un-patterned NbTiN nanowire showing a critical current of 14.8 µA at an operating temperature of 4.2 K.

Recall that for a temperature below its critical temperature, the superconducting nanowire will conduct a DC current without resistance when that said current is below the critical current of the nanowire. Like critical temperature, the critical current also depends on thin film material and wire dimensions. During the I-V characterization, we would expect to see zero voltage across the nanowire while the bias current is less than the critical current as the resistance of the nanowire is effectively zero in this current range. The gradient of the voltage applied vs. bias current yields the resistance of the contact pads, gold wire bonding, and printed circuit board that electrically connects the nanowire. This uniform resistance is observed up to the critical current when the bias current suddenly drops off because of a sudden increase in resistance of the nanowire as it exits the superconducting mode. The critical current observed in our expereiments was 14.8 µA. This value falls in the middle range of critical currents for nanowires of this material and dimensions with optimal 180^0 bends[44]. Figure 3-14 shows the results of these measurements taken with no incident photons at the operating temperature of 4.2 K.

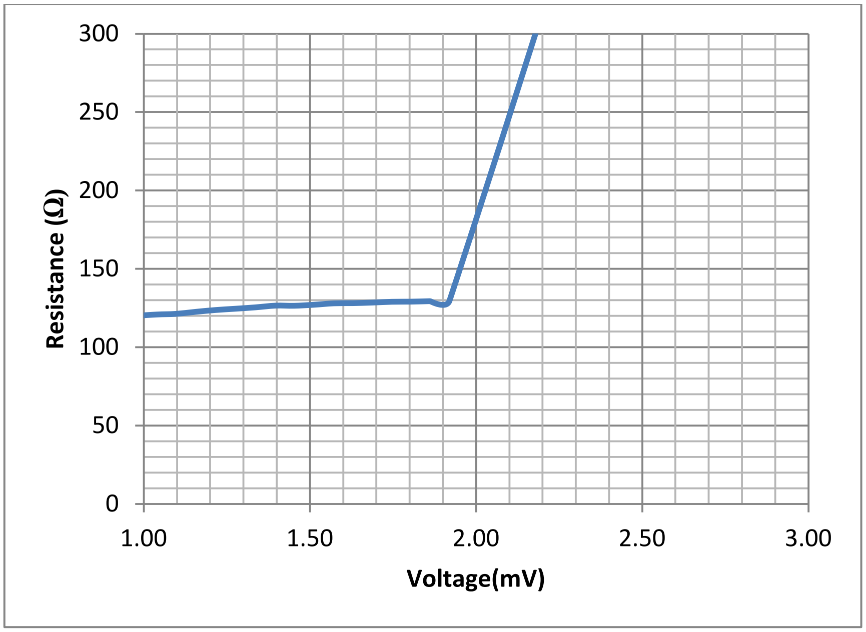

Figure 3-15: Experimental results for DC characterization showing the change in resistance with increasing voltage applied to the un-patterned nanowire.

In figure 3-15, we can see how the resistance due to peripheral connections plateau's at approximately 130 Ω before the critical current is surpassed causing the resistance of the nanowire to suddenly increase causing total resistance of the system to suddenly increase.

3.3.4 Overall setup with Matlab for automation

In these, experiments the apparatus shown below in figure 3-16 were used. The voltage pulses generated as a result of photo responses or DC characterization were amplified by the Phillips Scientific 6954 RF amplifier. The resulting signal is split by a microwave power splitter and the signals are sent to the oscilloscope and photon counter(SR400). MATLAB run time code was developed by our group to execute these experiments, both for the optoelectronic and DC characterization. The threshold voltage level and sampling time, for the photon counter are set after examining the nanowire response profile. For example, the threshold value is typically 30% of the amplitude of the response profile for the nanowire being characterized.

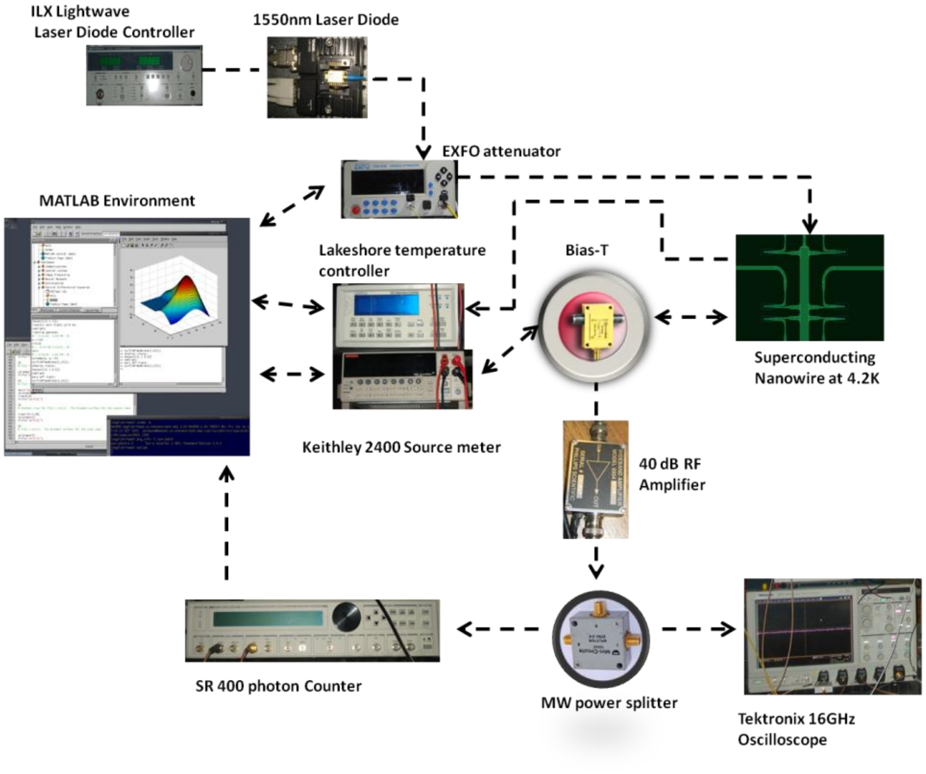

Figure 3-16: The experimental setup for single photon characterization of SNSPD

Chapter 4

Optoelectronic performance of the un-patterned NBTiN Superconducting nanowire on SIO$_2$

4.1 Count rate and Dark counts

Because the absorption of an un-patterned nanowire is much less than one, the detection efficiency as a function of just absorption for the single un-patterned nanowire will be much less than one as well. However, detection as function of absorption for the single un-patterned nanowire and count registration relative to the number of photons arriving at the nanowire surface, does give you an idea of the quantum efficiency of the wire. The term quantum efficiency of the single nanowire and detection efficiency are often used interchangeably. For this report we will stick with the terminology of detection efficiency, which for the single nanowire equates to the latter definition. To get as high a number of single photons possible in our lab setup arriving at the surface of the nanowire, a more powerful continuous wave (CW) source as opposed to the id-300 pulsed laser source was used

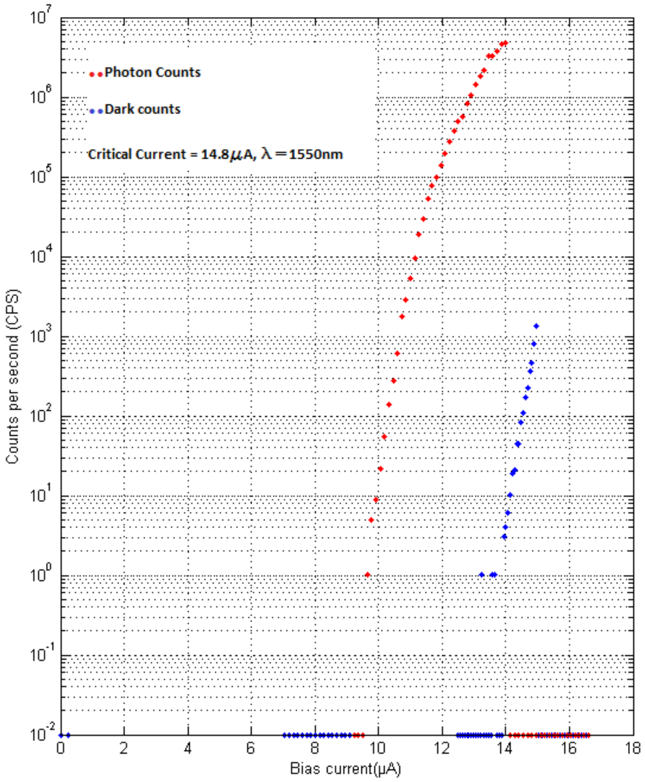

Figure 4-1: Experimental results for SNSPD photon count and Dark count vs bias current

to characterize the un-patterned single nanowire. The un-patterned nanowire optoelectronic characteristics are clearly and easily observed with this setup. Recall that, meander absorption efficiency, $\eta_{absorption}$ is a function of fill factor and absorption probability of the un-patterned nanowire. And count registration efficiency $\eta_{registering}$ is the portion of photons absorbed that are actually registered as counts. However, our purpose here is not to experimentally verify the low absorbtion efficiency of the single un-patterned nanowire, but to ensure that a single un-patterned nanowire with an optimal 180^0 bend with 300 nm spacing will show good photo response close to the critical current without latching and with minimal dark count in our packaging. Such a result will bode well for the detection efficiency of a SNSPD meander made with the same wire dimension and bending characteristics mentioned earlier, given a high filling factor for the meander after fabrication. Our approach allows us to fulfill the main purpose of this report i.e. to test the packaging performance and provide information for a future SNSPD meander design to be implemented in potential QKD experiments.

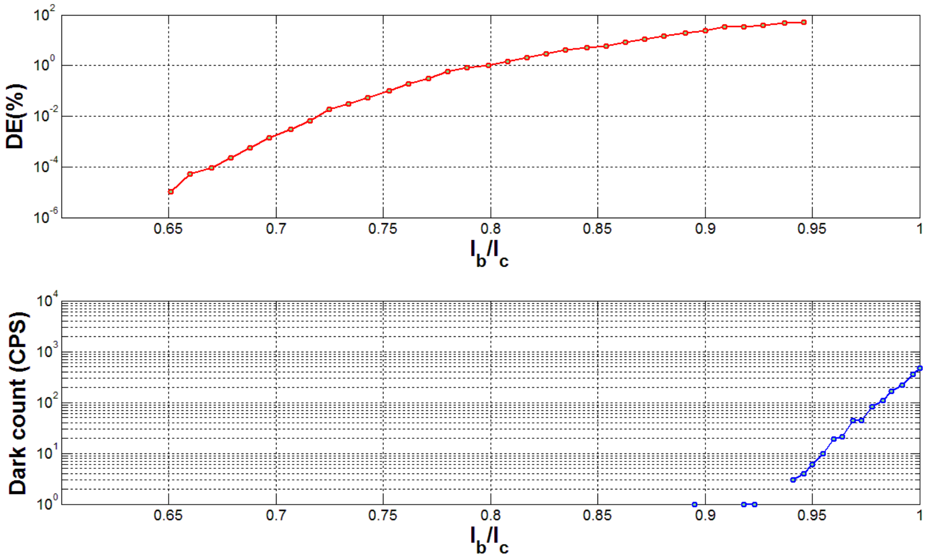

Figure 4-2: Experimental results for Detection efficiency and dark count of the NbTiN nanowire vs. bias to critical current ratio

The (CW) laser is routed through the EXFO variable attenuator at this point the shutter is on, and remains on until the dark count profile of the nanowire is complete as shown in figure 4-1. The count rate was measured for the NbTiN superconducting un-patterned nanowire and its variation with bias current. This was done at the 1550 nm wavelength, which is the single wavelength of interest in this report. These experiments were performed at the most ideal operating temperature possible, 4.2 K, given our setup. First, a DC sweep is done for dark counts ranging from zero to 120% of the full critical current. This range is determined during the IV characterization. Figure 4-1, shows that the dark count is approximately 0.01counts/sec from bias current, $I_b = 0\ \mu A$ up to $I_b = 13.87\ \mu A$ i.e 93.7% of the critical current. At 94.1% of the critical current i.e. $I_b = 13.93\ \mu A$, the dark counts start to increase almost linearly with I_b, beginning with 1count/sec and reaching a maximum of 1321 counts/sec at 101% of the critical current i.e. $I_b = 14.96\ \mu A$. The nanowire begins to latch beyond this point and the dark count drops off to zero. This nanowire DCR is excellent; at 95% critical current i.e. $I_b = 14\ \mu A$ the dark count is just 3counts/sec.

The attenuation level is now set to -11 dB to allow photons to arrive at the surface of the nanowire at a high rate. Simultaneously, the photo response is observed by resetting the bias current to $I_b = 9.23\ \mu A$ and increasing it in steps of 1% of critical current i.e. $I_b = 0.148\ \mu A$ up to 120% of the critical current. After $I_b = 14\ \mu A$ i.e. 95% of the critical current, the nanowire begins to latch. And the counts drop off to zero. The detection efficiency of the nanowire increases as the bias current approaches the critical current allowing more counts/sec to be recorded. However, the detection efficiency of the nanowire begins to saturate and level off at its maximum possible detection efficiency as the bias current approaches the critical current. A maximum detection rate of 4.86×10^6 counts/sec is observed. The count first increases from 0.01count/sec at approximately 65% of the critical current.

Note that photon counts are measured by subtracting the expected dark counts at the corresponding bias current values. Single photon sensitivity is verified through the proportional relationship between photon counts and incident photons[44]. Figure 4-2, shows the detection efficiency and dark count of the nanowire. The detection efficiency of the single nanowire peaks at 50.9%, the dark counts at this value are just 3 CPS.

4.2 Simulations of system efficiency for a square nanowire meander based on coupling efficiency range

4.2.1 Coupling to a nanowire meander

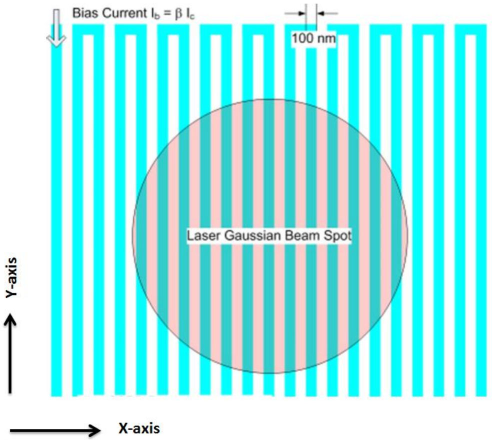

Figure 4-3: SNSPD drawing showing an ideal laser Gaussian beam spot incident the active area of square meander with 90^0 bends[49]

$Fiber\ core\ diameter \approx 9\ \mu m$

$Numerical\ Aperture\ (NA) \approx 0.13$

$Mode\ Field\ Diameter\ (MFD) at\ 1550nm \approx 10.5\mu m$

Figure 4-3, illustrates the spot size of the Gaussian beam originating from the SMF 28 fiber optic ferrule a distance z away on a square SNSPD meander. For the meander, the fraction of power incident on a square area is given by K[50].

Where;

$$\boldsymbol{K = \frac{2}{\pi\omega(z)^2}\iint_{-\frac{a}{2}}^{\frac{a}{2}} \exp\left(\frac{-2(x^2+y^2)}{\omega(z)^2}\right) dx\, dy} \qquad (4.1)$$

This can be further approximated as;

$$\boldsymbol{K = \frac{2}{\pi\omega_0^2\left(1+\left(\frac{\lambda z}{\pi\omega_0}\right)^2\right)}\iint_{-\frac{a}{2}}^{\frac{a}{2}}\exp\left(\frac{-2(x^2+y^2)}{\omega_0^2\left(1+\left(\frac{\lambda z}{\pi\omega_0}\right)^2\right)}\right)dx\,dy} \qquad (4.2)$$

4.2.2 Variation of coupling efficiency with distance from source

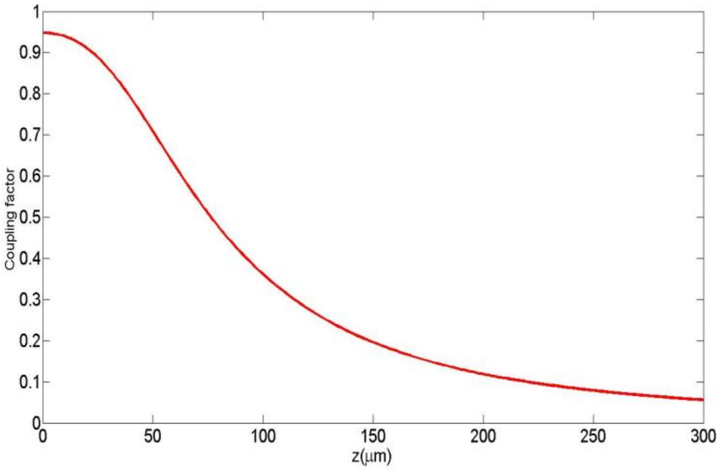

Figure 4-4 Simulated coupling factor of incident power in a 10 μm x 10 μm meander area vs. distance, z(μm) for wavelength, λ = 1550 nm assuming perfect alignment.

Having done our IV and photo response characterization we accept the validity of using the optimal 180^0 bend to design our nanowire meander. Therefore, for a typical square nanowire meander with dimensions 10 μm x 10 μm, and wire thickness of 8 nm and width of 100 nm with 180^0 bends with 300 nm spacing we see the simulated coupling profile illustrated in figure 4-4. We see a maximum coupling efficiency of 94.82% at 1550 nm.

We now consider lateral misalignment of the fiber ferrule that may likely occur as the packaging is cooled down to 4.2 K. where at this point K becomes;

$$\boldsymbol{K = \frac{2}{\pi\omega_0^2\left(1+\left(\frac{\lambda z}{\pi\omega_0}\right)^2\right)}\iint_{-\frac{a}{2}}^{\frac{a}{2}}\exp\left(\frac{-2((x-\delta x)^2+(y-\delta y)^2)}{\omega_0^2\left(1+\left(\frac{\lambda z}{\pi\omega_0}\right)^2\right)}\right)dx\,dy} \qquad (4.3)$$

The lateral misalignment is offset to some degree δx or δy in the x or y direction, respectively. Figure 4-5 shows the effect of this misalignment.

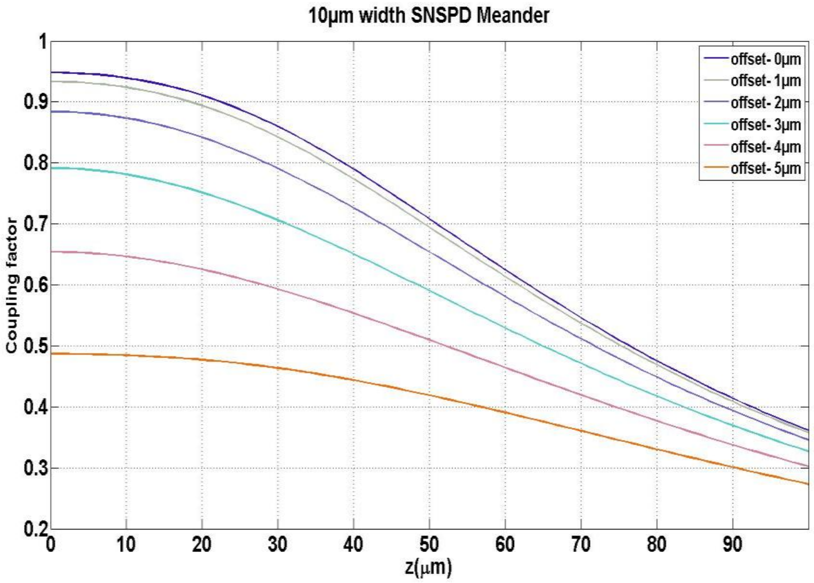

Figure 4-5: Simulated coupling factor of incident power in a 10 µm x 10 µm meander area vs. distance, z(µm) for wavelength, λ = 1550 nm with lateral offsets in the x or y direction.

However, note that invar 36 has very slow and steady thermal expansion changes with declines from room temperature to 4.2K. The stability in alignment due to the use of this metal for the packaging was demonstrated previously to be negligible[4]. With a maximum offset of 5 µm in either the x or y we see a maximum coupling factor of just 48.69%. However, touching the meander with the ferrule i.e. (z=0 µm) is impractical because of wire bonding and the potential electrical short that can be created by pressing the ferule against the meander. Therefore, based on the ~300 µm sensitivity of our vertical adjustment screw, we assume a minimum repeatable sensitivity adjustment of ¼ turn of the screw i.e. 75 µm. As a result, we get a maximum coupling factor of just 34.5% at 5 µm offset and a maximum of 50% coupling at 0 µm offset.

The simulation results of figure 4-6 illustrates that if we increase the side length of the square meander; first to 13 µm, then to 16 µm we see an incremental increase in the coupling factor for a maximum offset of 5 µm at z=75 µm. figure 4-6, shows a maximum coupling at 5 µm offset at 51.6% and 67.2% at 13 µm and 16 µm square meander width, respectively.

However, note that for each incremental increase in width, equation 2.24 shows that kinetic inductance of the meander is proportional to wire length i.e. meander size. Therefore, we would expect incrementally slower response times and longer SNSPD dead times as we increase the meander width[51][52][53]. Nevertheless, at 13 µm width, devices have been fabricated that achieve a response rate of approximately 100 MHz. Nevertheless, increasing the length of the wire to achieve great active area size does introduce another problem in fabrication. The probability of introducing sharp bends and hence a constriction to current flow increases during the fabrication process. The effect of current crowding, as preciously outlined, is augmented[44]. Though not readily available, alternatives that allow you to increase the SNSPD without increasing nanowire length and thickness can be considered for future application. For example, surface plasmon antennas, where light can be coupled more efficiently into a narrow aperture where the SNSPD resides[54]. In addition, the still theoretical plasmonic superconducting nanowire single photon detector that leverages the plasmonic nature of the superconducting layer to increase the surface absorption of the arriving photons is another option[55]. Lastly, the use of the recently invented amorphous tungsten silicide (W0.75Si0.25, or WSi) SNSPD with SQE of ~93% at 1550 nm, with corresponding DCR of 1000 CPS, and timing jitter of ~150 ps with SNSPD resolution frequency as high as 25 MHz operating as high as 2 K is a viable option for future Quantum information applications, like ultra-long distance QKD[56].

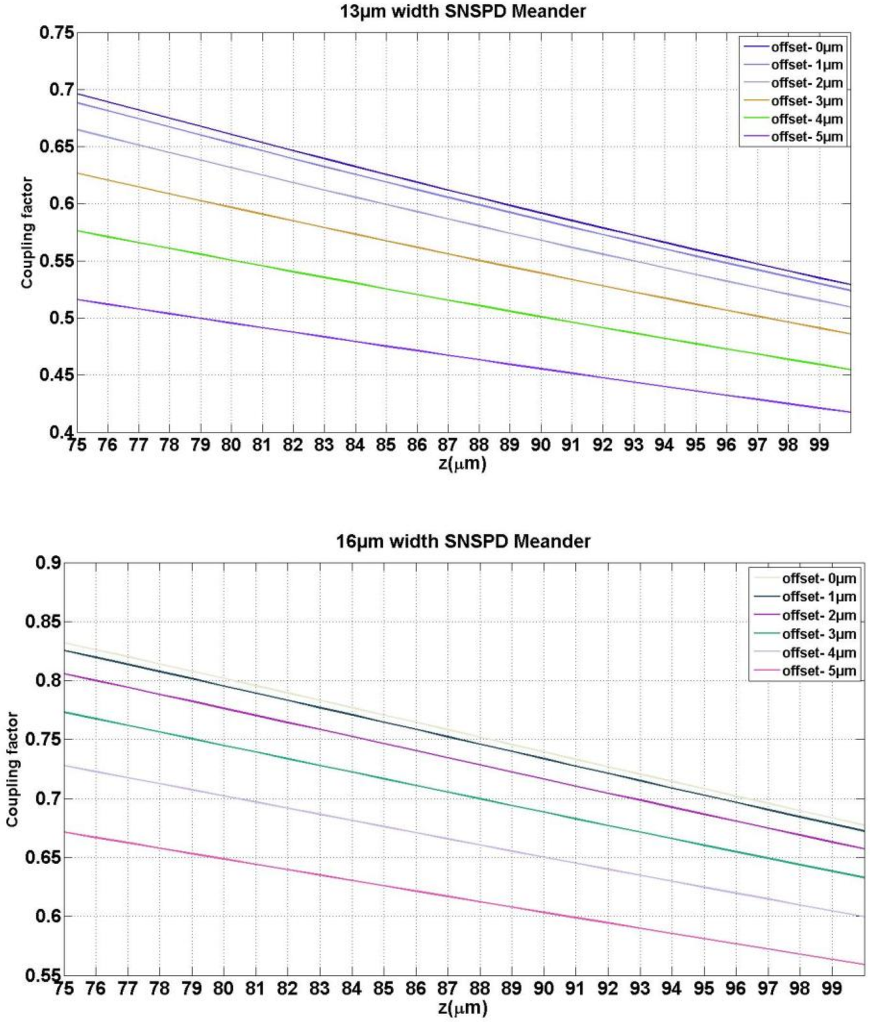

Figure 4-6: Simulated coupling factors of incident power in 13 μm x 13 μm and 16 μm x 16 μm meander areas vs. distance, z(μm) for wavelength, λ = 1550 nm with lateral offsets in the x or y direction.

Furthermore, SNSPD meander system quantum efficiency (SQE) is a function of coupling factor, K, and meander detection efficiency,η_{DE}[26]. Therefore, the SQE can be expressed as;

$$SQE = K \cdot \eta_{DE} \qquad (4.4)$$

$$Meander, \eta_{DE} = \eta_{absorption} \cdot \eta_{registering} \qquad (4.5)$$

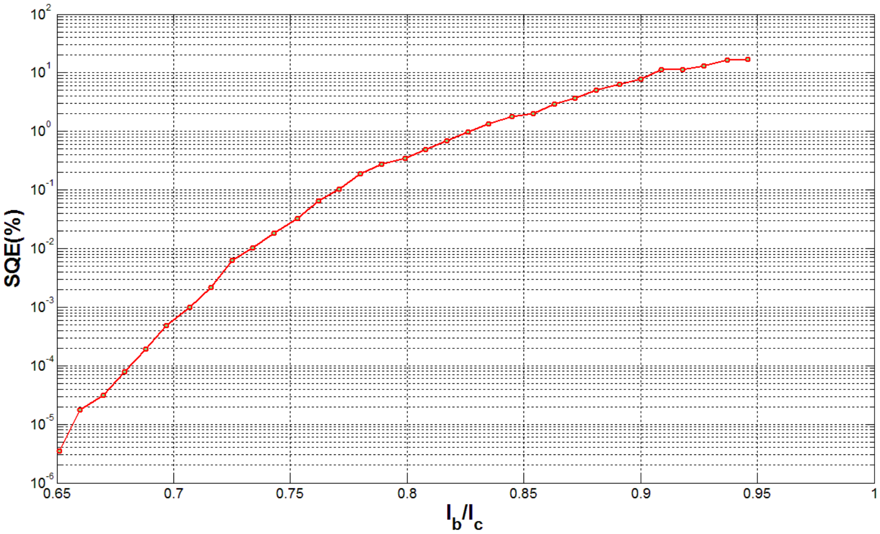

Figure 4-7: Simulated system quantum efficiency of 13µm wide square meander with good fill factor, ~0.65, optimal 180 bends with 300 nm spacing, and SQE of 0.52η_{DE} with 5 µm offset at 1550 nm assuming ideal fabrication with no constrictions.

Therefore, getting a 13 µm wide square meander with good fill factor, ~0.65 based on previous fabrications, and optimal 180 bends with 300 nm spacing will give at best SQE of 0.69η_{DE} with 0 µm offset and 0.52η_{DE} with 5 µm offset. However, note that a lateral offset in both the x and y direction simultaneously will lead to more drastic decreases in SQE. This must be avoided at all times with a single meander on an oxidized silicon substrate. Figure 4-7, shows a maximum reasonably expected SQE of 17%. The next step in our analysis is to now recommend the ideal SNSPD structural design for potential QKD applications.

In conclusion, thus far in this report we have demonstrated the following. In the next chapter we will discuss the optimal meander structure to be fabricated in future work. This structure will be shown to maximize system quantum efficiency of the packaged NbTiN SNSPD.

Our accomplishments are as follows:

- We have provided appropriate shielding from stray electromagnetic radiation (external contributor to DCR) through the use of the Invar 36 packaging
- We have designed a packaging with sufficient degrees of freedom to effectively couple to the optimal nanowire meander structure for the packaging developed in this work
- Our simulation and experimental results show very low DCR at 95% of the critical current with an expected SQE of 17% for a square meander with the NbTiN nanowire studied in this report

Chapter 5

Future work

In this report we have demonstrated through experiment that with optimal bending you can have good critical current, dark count rate and detection efficiency in a single un-patterned NbTiN nanowire. These findings were in sync with the previous findings of Akhlaghi et al.[44]. This bodes well for a SNSPD meander designed with the same wire geometry and material for use in quantum information implementations, such as QKD. These experiments also afforded the opportunity to verify the functionality of the packaging and cryogenic dipper stick design and fabrication for the packaging of both un-patterned nanowires and SNSPD meanders. Of course, the system quantum efficiency (SQE) of any SNSPD meander, and economical implementation of a SNSPD in QKD and other quantum information experiments, is solely dependent on effective packaging, and so this work greatly contributes to future experiments with SNSPD meanders of any type.

In this report, we also go on to suggest the optimal single SNSPD meander geometry for our Invar 36 packaging and stainless steel dipper probe. We have shown how the expected misalignment due to thermal expansion of the metal can affect SQE, and have simulated the expected SQE given the expected filling factor of ~0.65 based on past NbTiN SNSPD meander fabrications and expected optical coupling deficiencies with an alignment offset error margin of $\pm 5\,\mu m$ in the x or y direction at an optimal fiber coupling distance of $75\,\mu m$.

The final step, is to design the optimal NbTiN SNSPD structure on oxidized silicon substrate that leverages that cavity like behavior of the oxidized silicon substrate as shown by Tanner et al.[15], and allows for higher alignment offset error margins, and higher maximum counting rate when the optical beam is spread evenly across the meanders while boosting or maintaining the previously recommended SQE of ~17% based on our simulations. We will also simulate how this optimal meander structure performs in long distance QKD experiments given an overall optimal experimental setup. The QKD model discussed in section 1.3.2 will be revisited.

5.1 Potential NbTiN SNSPD meander structure to maximize system efficiency

The structure depicted in figure 5-1 would use the same NbTiN nanowire specifications of the nanowire characterized in this report. The structure will sit on a SiO_2 layer of thickness, Δd, such that $\lambda = 4n_{SiO2}\Delta d$ where $\lambda = 1550\,nm$ and $n_{SiO2} \approx 1.45$. Cavity like behavior will be observed as extra reflections occur at the SiO_2/Si boundary; this will maximize constructive interference at this wavelength at the surface of the meander structure and boost absorption, as explained in section 2.3.2.

There are two ways in which we can utilize the structure depicted in figure 5-1. First we can package it using the fabrication reported in this thesis. This means we will be able to connect one or two of the meanders in parallel. And the approach will be too align the ferrule with the center of the packaging at room temperature, then step by step connect different pairs of meanders to our current source and readout electronics and perform optoelectronic characterization until the meander pair with the highest efficiency is found. The result is an increase in the prior off-center misalignment error tolerance of $\pm 5\ \mu m$ in the x or y direction; this configuration allows up to $\sim 18\ \mu m$ offset in the x-direction and 5 μm offset in the y-direction and vice versa. With 100 nm spacing or less between the adjacent meanders you would expect a quantum efficiency of at least 17% within the latter mentioned offset range, with a coupled SMF 28 fiber at $75\ \mu m$ away, as you will be doubling the active area.

However, beyond the greater margin of error for fiber misalignment there are other advantages to connecting two SNSPDs in parallel on a single substrate with little or no disadvantages as well. Dauler et al.[57],[58],[59] have already explored the deficiencies and benefits of such a SNSPD structural design when the multi-element meander structure is connected one meander pair at a time. This was shown, using NbN nanowires 100 nm wide and 4nm thick with 4 µm x 4.2 µm meander pairs on sapphire substrate. The meanders were 100 nm apart. At 1550 nm wavelength the elements were biased at 95% of their respective critical currents. There work shows that critical currents of the meander pair in parallel remain the same together as they were when connected individually. However, when one SNSPD is biased beyond its critical current and heat is continually dissipated in one of the meanders, the adjacent meander sees a slight decrease in its critical current (~10%) because of local heating. In addition, with < 1 ps optical pulses at 1550 nm wavelength at a repetition rate of 10 MHz, the timing jitter of the pairs were inspected. It was found that the timing jitter for the pair closely matches the convolution of the individual timing jitters indicating that each meander timing jitter is independent. Moreover, cross talk due to noise induced in one element due to a detection event in the other element was negligible as total noise in the adjacent elements remained within its expected range. Furthermore, detection efficiency (DE) was investigated to see how any interaction might add or detract from the efficiencies of the individual meanders. It was found that there is no difference in DE when one or both adjacent meanders are biased at 95% of critical current. Therefore, the conclusion is that there is no interaction between the adjacent meanders in the pair as critical current, timing jitter, noise, and DE remain the same for each meander.

The benefits of the recommend structure include, an increase in speed by a factor of two due to the presence of individual meanders counting independently, assuming even distribution of the optical beam on both meander areas. This has been previously demonstrated and measured with respect to the probability of detecting a second optical pulse as a function of time after detecting an initial optical pulse[57]. In addition, photon number resolution becomes possible when we have multiple elements connected in parallel, but it is shown that the expected photon number resolution for a pair of meanders will be lower than that of more than two meanders in parallel and just sufficient for most optical communication and quantum optics applications, but not linear optics quantum computing[59].

The second approach to using the 9 multi-element SNSPD meander structure is much simpler, and involves no packaging as reported in this thesis, but theoretically can yield better results. This would involve placing the coupled fiber some distance, z (m), away from the meander structure such that the incident Gaussian beam spot size $\omega(z) \ll A,$ the combined active area of the 9 meanders. With the 9 meanders all connected in parallel you would expect a coupling factor of at least 90% based on the coupling model discussed in section 4.2.1. Hence a SQE, $\geq 0.9\eta_{DE}$ i.e. at least 29% is expected. In addition, with 9 independent meanders you would expect better photon number resolution.

However, it is not yet known how connecting 9 SNSPDs in parallel on a single substrate might affect the total noise level of the system. This is a key factor in implementations like QKD. This might be something worthy of future investigation.

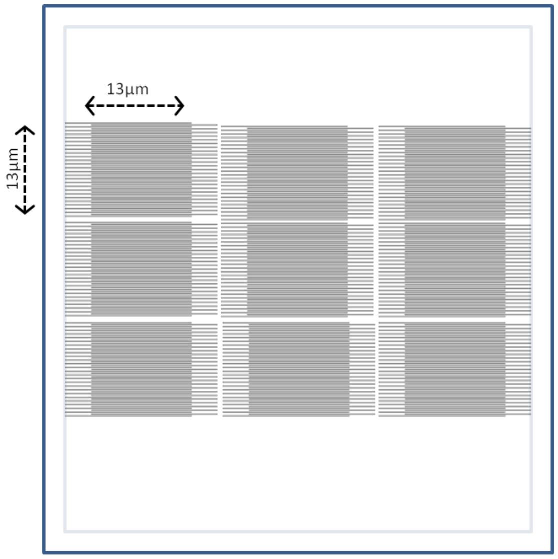

Figure 5-1: A 3×3 matrix of 13 μm $\times$ 13 μm NbTiN SNSPD square meanders with optimal 180 degree bends, 300 nm spacing, and 8 nm wire thickness. A filling factor of ~0.65 per meander is assumed with spacing between adjacent meanders of 100 nm or less on an oxidized silicon substrate.

In conclusion, assuming typical jitter range of (<100ps) for any future SNSPD fabrication, we have taken steps to ensure that our packaging and optimal meander structure facilitate the most important requirements for quantum information applications outlined in section 1.3.5, especially QKD. As previously stated:

- We have provided appropriate shielding from stray electromagnetic radiation (external contributor to DCR) through the use of the Invar 36 packaging
- We have designed a packaging with sufficient degrees of freedom to effectively couple to the optimal nanowire meander structure for the packaging developed in this work
- We have designed the optimal meander structure to maximize system quantum efficiency of the packaged NbTiN SNSPD
- Our simulation and experimental results show very low DCR at 95% of the critical current with an expected SQE of 17% for a square meander with the NbTiN nanowire studied in this report

To further decrease any external contribution to jitter where entangled photon pair arrival rates exceed 1GHz at the receiving end, we recommend a higher bandwidth RF amplifier than the one used during the characterization process. This is because the limited band width of the Phillips scientific is just 100 KHz to 1.8 GHz. We also recommend the use of low loss (ULL) fiber as opposed to regular fiber as the exponential loss along the channel be mitigated in ULL fiber, as shown in figure 5-2, compared to the SMF 28e fiber optic cable demonstrated in figure 1-4.

5.2 Future system requirements for QKD over 400km using SNSPD and NFAD detectors

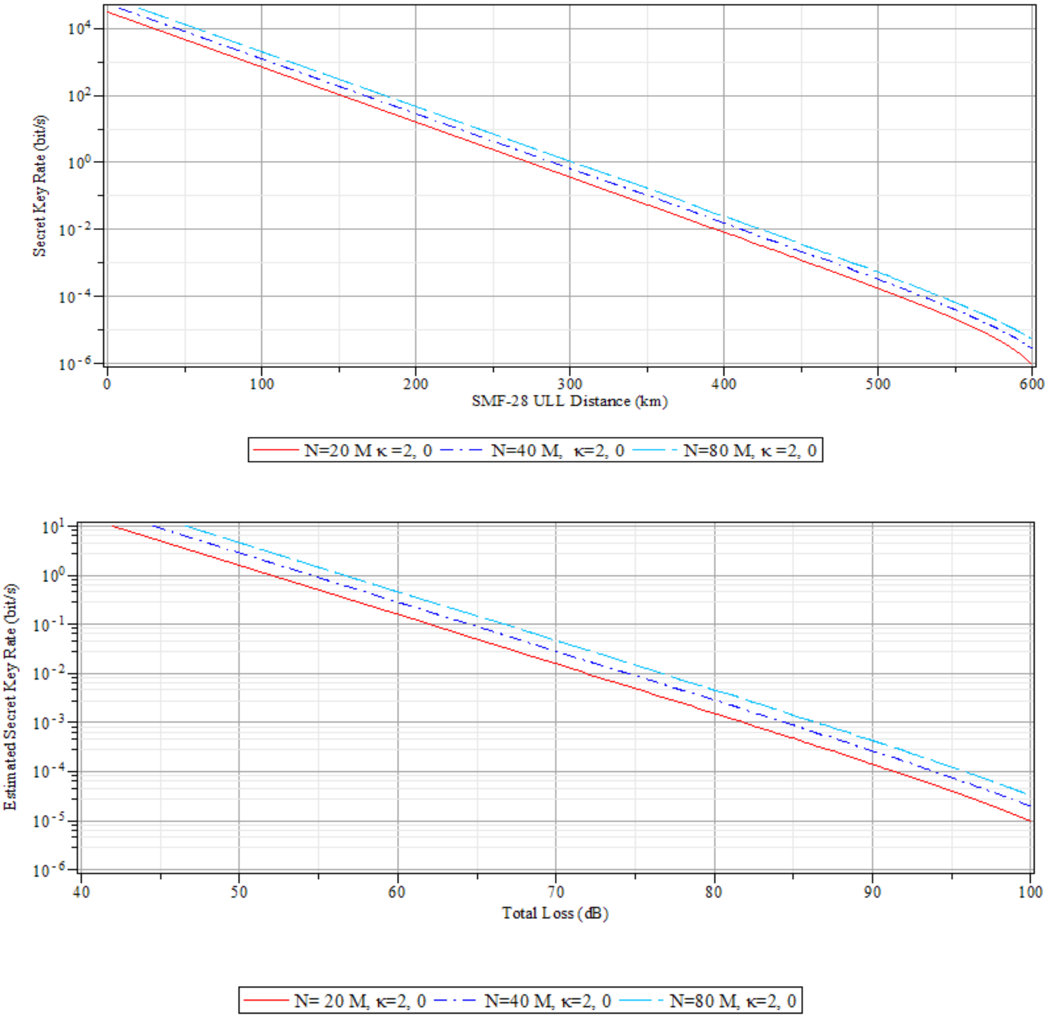

Figure 5-2: Simulation of secure key rate versus distance (top) and secure key rate versus fiber attenuation (dB) (bottom) in SMF-28 fiber for a QKD scheme with a symmetrical, spectrally correlated source using an NFAD and SNSPD for entangled single photon detection. The secure key rate is plotted for BBO crystal pair generation, N at 20 MHz, 40 MHz, and 80 MHz. After pulsing is set at 2% for the NFAD; 0% for the SNSPD. $\eta_{SNSPD} = 17\%, \eta_{NFAD} = 8\%, DCR_{SNSPD} = 39\ CPS, DCR_{NFAD} = 100\ CPS.$

5.2.1 Necessary specifications for spectrally correlated entangled photon source

The Quantum Photonics Laboratory at the Institute for quantum computing has developed a spectrally correlated entangled single photon source for QKD over long distances[20]. The optimal pair generation rate has not yet been determined. However, the current maximum pump rate is at 80 MHz. At this frequency many higher order pairs that adversely impact the security of any entanglement asked QKD protocol are being produced[17]. Therefore, a lower optimal pump rate for this source must first be found. The spectrally entangled photon source will need to produce as many single photon pairs as possible without producing too many higher order pairs. My simulations assume this optimal rate will lie in the range of 20-80 MHz, though it can be much lower. In addition, the current coupling loss of -13 dB will need to be mitigated for achieving the highest possible secure bit rate at the optimal pump rate. A coupling loss factor closer to -3 dB is assumed in the simulation shown in figure 5-2.

5.2.2 Necessary specifications for NFAD detector

The current specifications for the negative feedback avalanche diode (NFAD) single photon detector are 8% efficiency, DCR of 100 CPS, after pulsing at 4%. The after pulsing adds a significant amount of noise to the system and will prohibit its performance when precise, high rate localization of incoming photons is needed in QKD. A NFAD detector with 2% or less after pulsing will be most optimal and is taken into consideration in the simulation shown in figure 5-2.

Appendix A

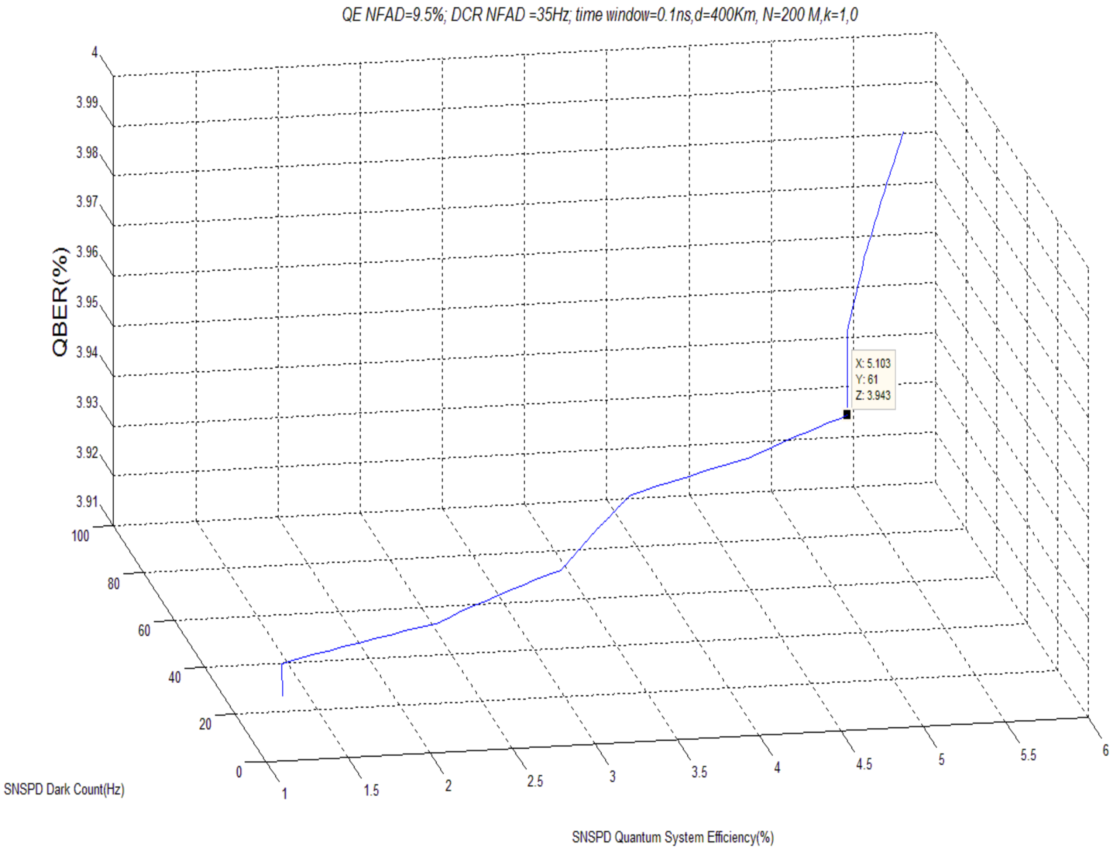

Figure A- 1: Simulation that demonstrates that with incremental changes in quantum efficiency with very ideal setting for the NFAD detector, the absolute minimal desired SQE and maximum DCR are 5.103% and 61 Counts per second respectively for the NbTiN SNSPD. The NFAD is set to a DE of 9.5%, DCR of 35 counts per second with an ideal source pair generation rate of 200 MHz.

Figure A-1 shows that with a time window of 100ps (0.1ns) and NFAD detector efficiency of 9.5% with a DCR of 35 counts per second we would get a rapid rise in QBER beyond a NbTiN SNSPD DCR of 61 CPS even if the SQE was increased beyond 5.103%. We therefore take a SQE of 5.103% and maximum DCR of 61 CPS and our minimum parameters for a packaged NbTiN SNSPD to be used in any future long distance QKD experiments (~400km). This can be thought of as the lower bound worst case performance for the NbTiN SNSPD. The upper bound worst case performance is given when we consider more non-ideal parameters for the NFAD detector. Figure A-2 shows that at the upper bound for QBER to perform QKD i.e. 14.6%, as highlighted in section 1.3.1, is reached when we take a more realistic time window of 156ps based on currently available technology and set the NFAD DE to 6% with a DCR of 100 counts per second and 4% afterpulsing. The resultant desired parameters for the NbTiN SNSPD are then at least 6.989% DE and at most 326 dark counts per second.

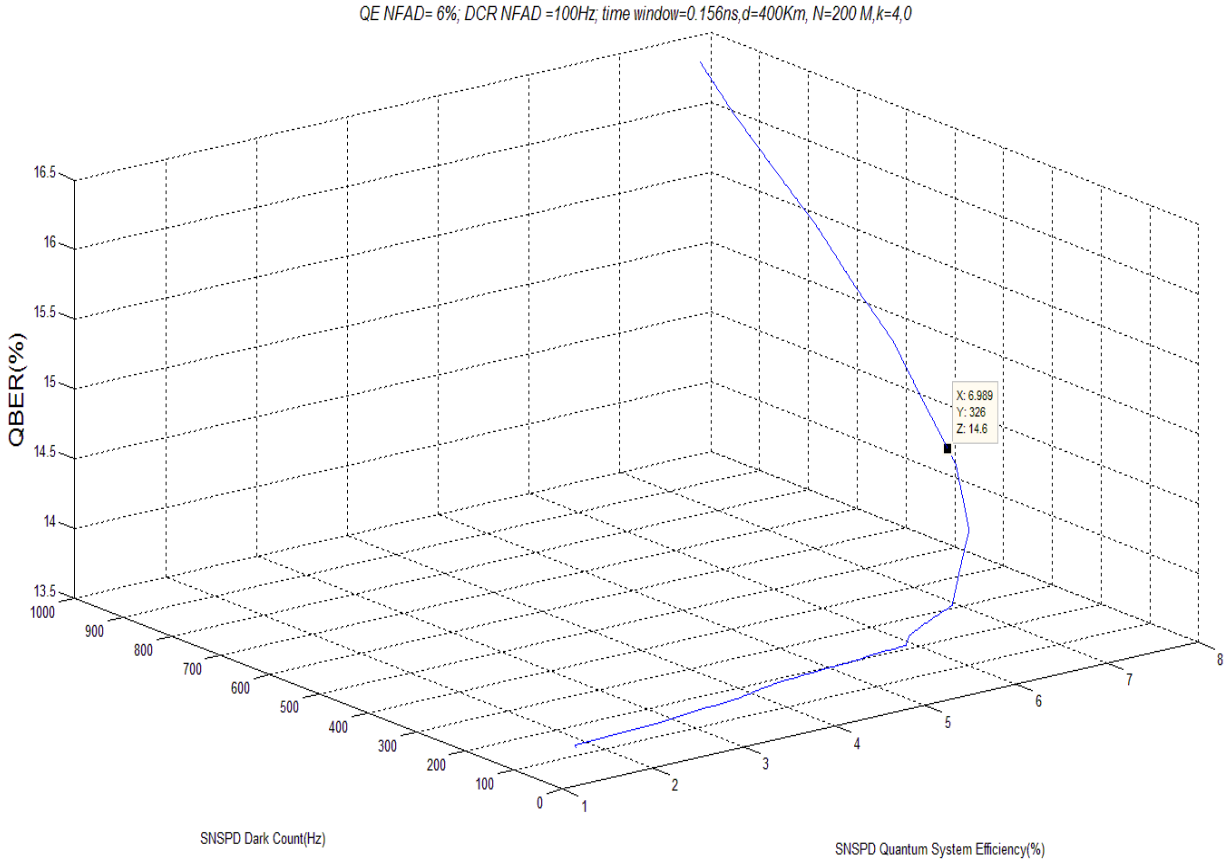

Figure A- 2: Simulation that demonstrates that with incremental changes in quantum efficiency with non- ideal setting for the NFAD detector, the upper bound worst case settings for DCR is 326 counts per second and at least 6.989% SQE for the NbTiN SNSPD. The NFAD is set to a DE of 6%, DCR of 100 counts per second with an ideal source pair generation rate of 200 MHz. NFAD afterpulsing is now at 4%.

The relationship for change in SQE vs DCR is based on experimental work done by Tanner et al.[15] on a NbTiN SNSPD meander with similar fabrication features to the one that is eventually recommended in this report. This relationship is shown in Figure A-3.

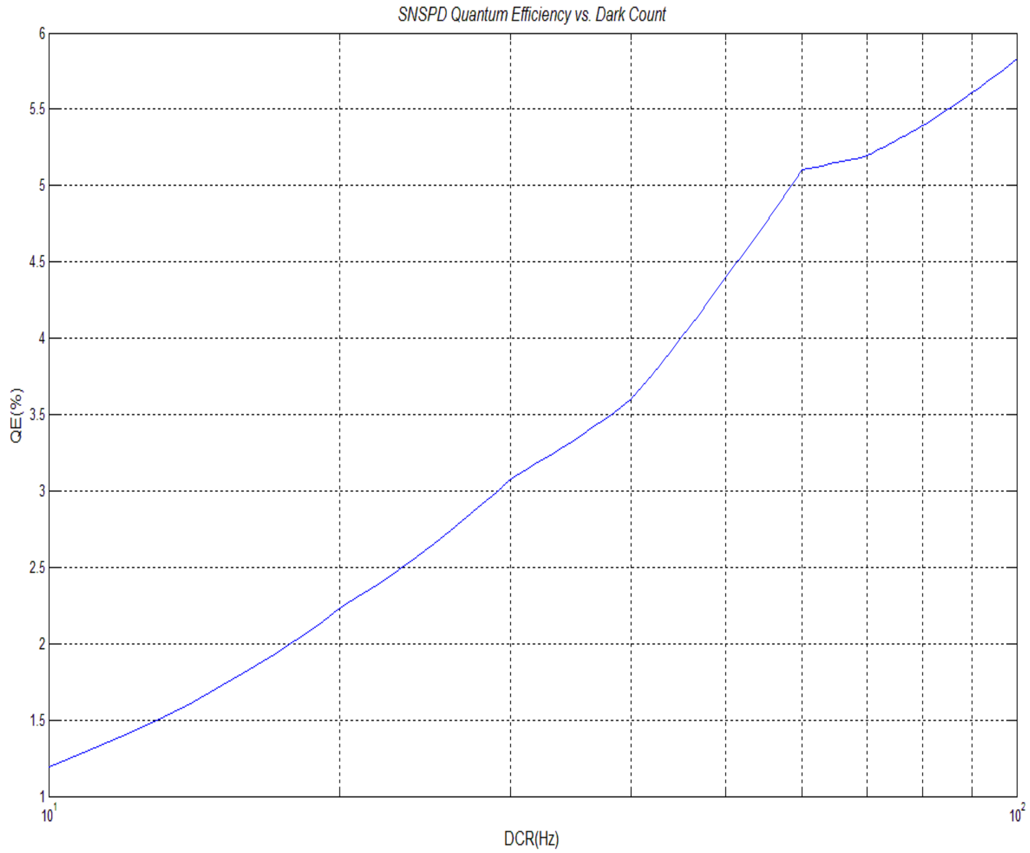

Figure A- 3: This demonstrates how SQE is changed with respect to DCR in figure A-1

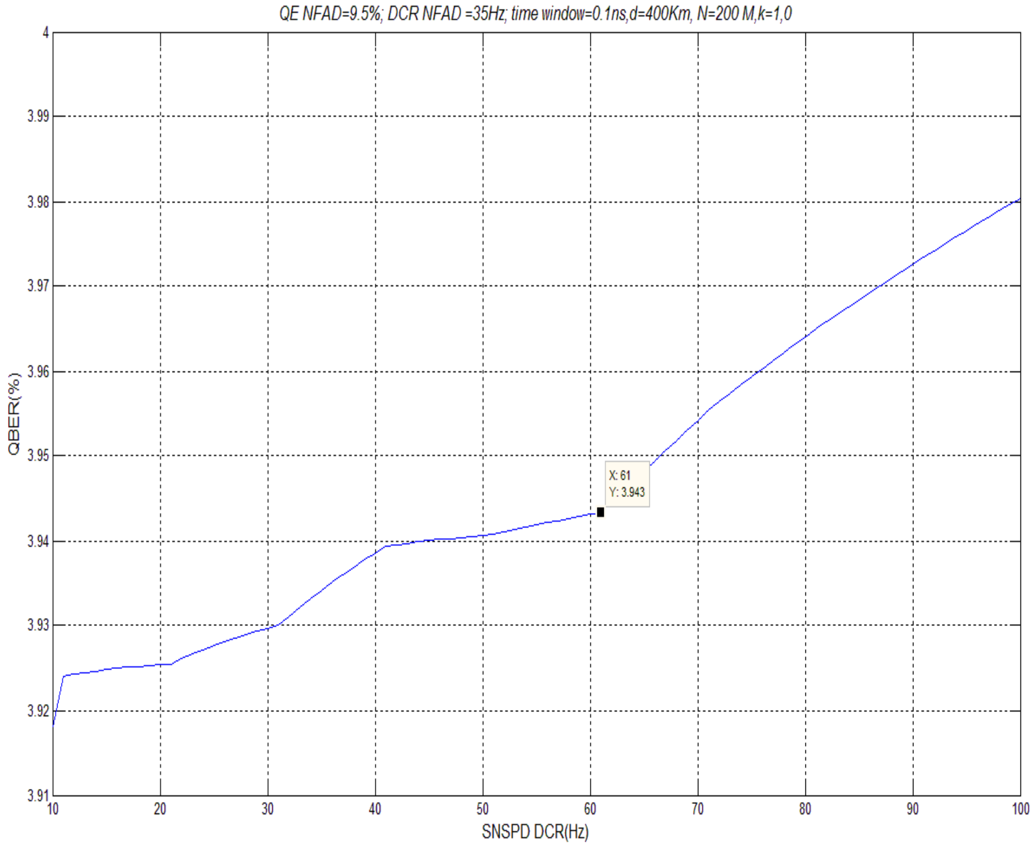

Figure A- 4: 2-D simulation of QBER vs DCR for the NbTiN SNSPD.

Figure A-4 further demonstrates how the partial rate of change of QBER with respect to DCR for the NbTiN SNSPD suddenly increases beyond 61 CPS.

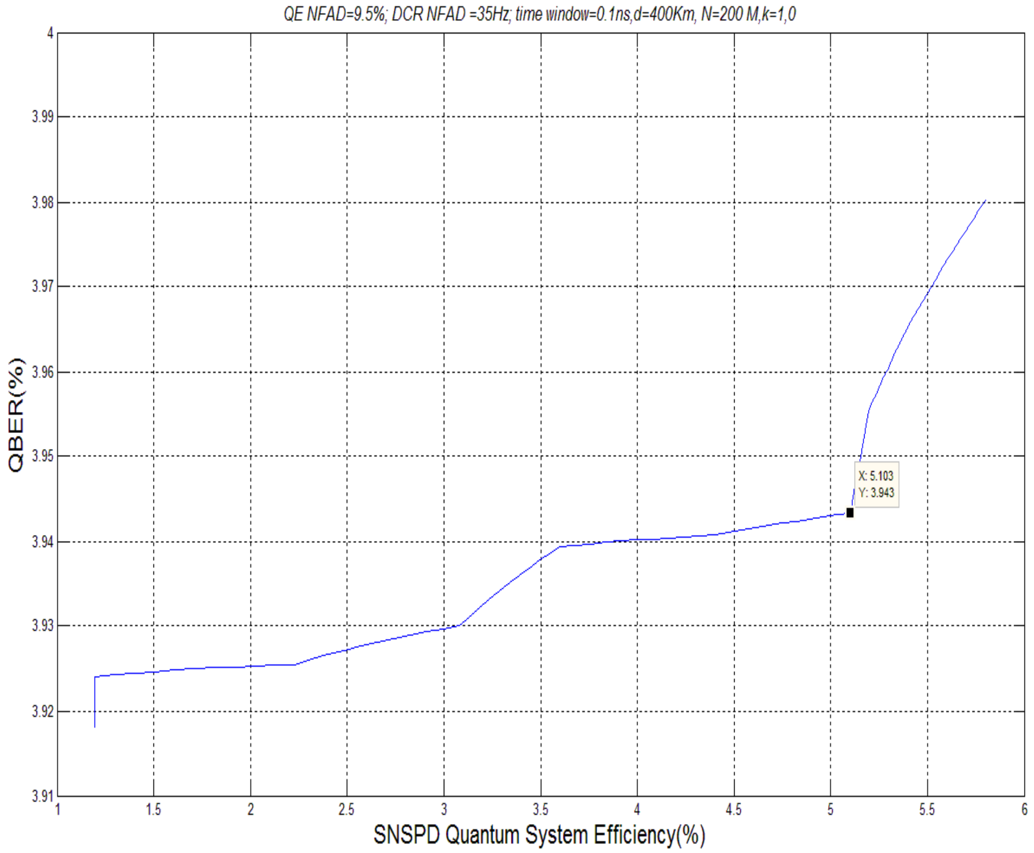

Figure A- 5: 2-D simulation of QBER vs DCR for the NbTiN SNSPD.

Figure A-5 demonstrates the partial rate of change of QBER with respect to SQE. The even more sudden rise here shows the impact that an increase in DCR beyond 61 CPS cannot be mitigated by continual gradual increases in the SQE. The required SQE would have to be much higher for NbTiN DCR above 61 CPS.

Setting #	η_NFAD[1]	η_SNSPD[2]	DCR_NFAD[1]	DCR_SNSPD[2]	κ_NFAD[1]	κ_SNSPD[2]	time window	N, MHz	R at 300KM (bits/s)	R at 400KM (bits/s)
1	9.5%	3.08%	35Hz	31Hz	1	0	0.156ns	100	2.00E-01	6.00E-03
2	**9.5%**	**3.08%**	**35Hz**	**31Hz**	**1**	**0**	**0.1ns**	**200**	**4.00E-01**	**9.00E-03**
3	3.8%	3.08%	10Hz	31Hz	0.1	0	0.156ns	200	2.00E-01	5.00E-03
4	3.8%	3.08%	10Hz	31Hz	0.1	0	0.10ns	300	3.00E-01	7.00E-03
5	9.5%	3.598%	35Hz	41Hz	1	0	0.156ns	100	3.00E-01	7.00E-03
6	**9.5%**	**3.598%**	**35Hz**	**41Hz**	**1**	**0**	**0.1ns**	**200**	**5.00E-01**	**1.00E-02**
7	3.8%	3.598%	10Hz	41Hz	0.1	0	0.156ns	200	2.00E-01	5.00E-03
8	3.8%	3.598%	10Hz	41Hz	0.1	0	0.10ns	300	3.00E-01	7.00E-03
9	**9.5%**	**5.103%**	**35Hz**	**61Hz**	**1**	**0**	**0.1ns**	**200**	6.60E-01	1.50E-02

Table A- 1: Summary of various simulation of secure bit rate, R, for different settings of detection efficiency and DCR for the NFAD and SNSPD used in tandem. The time window is varied along with the photon pair generation rate, N, until the best combination is found.

Table A-1, shows that at the minimal optimum setting for the NbTiN SNSPD combined with the ideal settings of the NFAD and entangled photon source previously mentioned, we can achieve a maximum of 0.66 bits/s over 300km QKD and .015 bits/s over 400km. Setting number 2 and 6 produce higher than average secure bit rates while setting 6 shows the parameters found in the previous simulations. It is not surprising that setting 6 produces the highest secure bit rates. In actual experimental conditions we would expect less ideal performance by both the NFAD and single photon source; therefore, to achieve the latter secure key rates we desire a SQE above 5.103% and DCR below 61 CPS for the NbTiN SNSPD. The pair generation rate, N is kept at 100 MHz or higher because this is the ideal minimum rate to ensure actual QKD without consideration of the finite size effect. One can ignore this effect when the pair production rate is in the region of hundreds of megahertz[6].

Bibliography

[1] A. J. Annunziata, “Single-Photon Detection , Kinetic Inductance , and Non-Equilibrium Dynamics in Niobium and Niobium Nitride Superconducting Nanowires,” Yale University, 2010.

[2] R. H. Hadfield, “Single-photon detectors for optical quantum information applications,” *Nature Photonics*, vol. 3, no. 12, pp. 696–705, Dec. 2009.

[3] G. Ribordy, J. D. Gautier, H. Zbinden, and N. Gisin, “Performance of InGaAs/InP Avalanche Photodiodes as Gated-Mode Photon Counters.,” *Applied optics*, vol. 37, no. 12, pp. 2272–7, Apr. 1998.

[4] J.Orgiazzi, “Packaging and Characterization of NbN Superconducting Nanowire Single Photon Detectors,” University of Waterloo, 2009.

[5] A. R. Dixon, Z. L. Yuan, J. F. Dynes, a W. Sharpe, and a J. Shields, “Gigahertz decoy quantum key distribution with 1 Mbit/s secure key rate.,” *Optics express*, vol. 16, no. 23, pp. 18790–7, Nov. 2008.

[6] Z. Yan, “An Ultra Low Noise Telecom Wavelength Free Running Single Photon Detector Using Negative Feedback Avalanche Diode,” pp. 1–25.

[7] X. Jiang, M. a. Itzler, K. O’Donnell, M. Entwistle, and K. Slomkowski, “InGaAs/InP Negative Feedback Avalanche Diodes (NFADs),” *SPIE*, vol. 8033, p. 80330K–80330K–9, May 2011.

[8] G. Gol, A. Korneev, O. Minaeva, I. Rubtsova, I. Milostnaya, G. Chulkova, B. Voronov, K. Smirnov, V. Seleznev, W. Słysz, J. Kitaygorsky, A. Cross, A. Pearlman, and R. Sobolewski, “Superconducting nanostructured detectors capable of single-photon counting in the THz range,” pp. 555–557.

[9] A. E. Lita, A. J. Miller, and S. W. Nam, “Counting near-infrared single-photons with 95% efficiency,” *Optics Express*, vol. 16, no. 5, pp. 3032–3040, 2008.

[10] G. Fujii, D. Fukuda, T. Numata, A. Yoshizawa, H. Tsuchida, S. Inoue, and T. Zama, “Fiber Coupled Single Photon Detector with Niobium,” in *Quantum Communication and Quantum Networking*, 2010, pp. 220–224.

[11] A. Korneev, O. Minaeva, A. Divochiy, A. Antipov, N. Kaurova, V. Seleznev, B. Voronov, G. Gol’tsman, D. Pan, J. Kitaygorsky, W. Slysz, and R. Sobolewski, “Ultrafast and high quantum efficiency large-area superconducting single-photon detectors,” vol. 6583, p. 65830I–65830I–9, May 2007.

[12] V. Anant, A. J. Kerman, E. A. Dauler, K. W. Joel, K. M. Rosfjord, and K. K. Berggren, “Optical properties of superconducting nanowire single-photon detectors Abstract :,” *Optics Express*, vol. 16, no. 14, pp. 46–52, 2008.

[13] A. Korneev, A. Divochiy, Y. Vachtomin, Y. Korneeva, I. Florya, M. Elezov, N. Manova, M. Tarkhov, P. An, A. Kardakova, A. Isupova, G. Chulkova, K. Smirnov, N. Kaurova, V. Seleznev, B. Voronov, and G. Goltsman, "Recent advances in superconducting NbN single-photon detector development," *SPIE,* vol. 8072, pp. 807202–807202–10, May 2011.

[14] S. N. Dorenbos, E. M. Reiger, U. Perinetti, V. Zwiller, T. Zijlstra, and T. M. Klapwijk, "Low noise superconducting single photon detectors on silicon," *Applied Physics Letters*, vol. 93, no. 13, p. 131101, 2008.

[15] M. G. Tanner, C. M. Natarajan, V. K. Pottapenjara, J. a. O'Connor, R. J. Warburton, R. H. Hadfield, B. Baek, S. Nam, S. N. Dorenbos, E. B. Ureña, T. Zijlstra, T. M. Klapwijk, and V. Zwiller, "Enhanced telecom wavelength single-photon detection with NbTiN superconducting nanowires on oxidized silicon," *Applied Physics Letters*, vol. 96, no. 22, p. 221109, 2010.

[16] L. Yu, R. K. Singh, H. Liu, S. Y. Wu, R. Hu, D. Durand, J. Bulman, J. M. Rowell, and N. Newman, "Fabrication of Niobium Titanium Nitride Thin Films With High Superconducting Transition Temperatures and Short Penetration Lengths," *IEEE Transactions on Appiled Superconductivity*, vol. 15, no. 1, pp. 44–48, Mar. 2005.

[17] W. Tittel, H. Zbinden, and N. Gisin, "Quantum cryptography," vol. 74, no. January, pp. 145–195, 2002.

[18] "Optical Fiber Attenuation | Fiber Optic Training & Tutorials - FAQ, Tips & News." [Online]. Available: http://www.fiberoptics4sale.com/wordpress/optical-fiber-attenuation/. [Accessed: 10-Feb-2013].

[19] M. F. Robert H Hadfield, Chandra Mouli Natarajan, (1) Burm Baek, Sae Woo Nam (2) Shigehito Miki and Z. W. (3) Masahide Sasaki, "Superconducting nanowire single-photon detectors for quantum key distribution," *presented at SECOQC Conf. [Online].*, 2008. [Online]. Available: http://www.secoqc.net/downloads/abstracts/SECOQC-Hadfield.pdf. [Accessed: 25-Jan-2013].

[20] T. Lutz, P. Kolenderski, and T. Jennewein, "decorrelated photon pairs at telecom wavelength," pp. 200–202.

[21] T. Scheidl, R. Ursin, A. Fedrizzi, S. Ramelow, X.-S. Ma, T. Herbst, R. Prevedel, L. Ratschbacher, J. Kofler, T. Jennewein, and A. Zeilinger, "Feasibility of 300 km quantum key distribution with entangled states," *New Journal of Physics*, vol. 11, no. 8, p. 085002, Aug. 2009.

[22] X. Ma, C.-H. Fung, and H.-K. Lo, "Quantum key distribution with entangled photon sources," *Physical Review A*, vol. 76, no. 1, p. 012307, Jul. 2007.

[23] R. H. Hadfield, M. J. Stevens, S. S. Gruber, A. J. Miller, R. E. Schwall, R. P. Mirin, and S. W. Nam, "Single photon source characterization with a superconducting single photon detector.," *Optics express*, vol. 13, no. 26, pp. 10846–53, Dec. 2005.

[24] W. Slysz, M. Wegrzecki, J. Bar, P. Grabiec, M. Gorska, E. Rieger, S. Dorenbos, V. Zwiller, I. Milostnaya, O. Minaeva, A. Antipov, O. Okunev, A. Korneev, K. Smirnov, B. Voronov, N. Kaurova, G. N. Gol'tsman, J. Kitaygorsky, D. Pan, A. Pearlman, A. Cross, I. Komissarov, and R. Sobolewski, "Fiber-coupled NbN superconducting single-photon detectors for quantum correlation measurements," vol. 6583, p. 65830J–65830J–11, May 2007.

[25] B. S. Robinson, A. J. Kerman, E. a Dauler, R. J. Barron, D. O. Caplan, M. L. Stevens, J. J. Carney, S. a Hamilton, J. K. W. Yang, and K. K. Berggren, "781 Mbit/s photon-counting optical communications using a superconducting nanowire detector.," *Optics letters*, vol. 31, no. 4, pp. 444–6, Feb. 2006.

[26] C. M. Natarajan, M. G. Tanner, and R. H. Hadfield, "Superconducting nanowire single-photon detectors: physics and applications," *Superconductor Science and Technology*, vol. 25, no. 6, p. 063001, Jun. 2012.

[27] R. Sobolewski, A. Pearlman, and G. Chulkova, "Ultrafast superconducting single-photon optical detectors," vol. 5123, no. 585, pp. 1–11, 2003.

[28] J. Zhang, W. Słysz, a. Pearlman, a. Verevkin, R. Sobolewski, O. Okunev, G. Chulkova, and G. Gol'tsman, "Time delay of resistive-state formation in superconducting stripes excited by single optical photons," *Physical Review B*, vol. 67, no. 13, p. 132508, Apr. 2003.

[29] N. W. Ashcroft and D. N. Mermin, *Solid State Physics*. Thomson Learning, 1976.

[30] A. J. Annunziata, D. F. Santavicca, L. Frunzio, G. Catelani, M. J. Rooks, A. Frydman, and D. E. Prober, "Tunable superconducting nanoinductors," *Nanotechnology*, vol. 21, no. 44, p. 445202, Nov. 2010.

[31] M. Tinkham, *Introduction to superconductivity*, 2nd Ed. Mineola, NY: Dover Publications, 1995.

[32] S. M. Anlage, J. Snortland, and M. R. Beasley, "A current-controlled variable delay superconducting transmission line," *IEEE Trans. Appl. Supercond.*, vol. 25, no. 1388, 1988.

[33] A. Korneev, P. Kouminov, V. Matvienko, G. Chulkova, K. Smirnov, B. Voronov, G. N. Gol'tsman, M. Currie, W. Lo, K. Wilsher, J. Zhang, W. Słysz, A. Pearlman, A. Verevkin, and R. Sobolewski, "Sensitivity and gigahertz counting performance of NbN superconducting single-photon detectors," *Applied Physics Letters*, vol. 84, no. 26, p. 5338, 2004.

[34] A. Engel, A. Semenov, H.-W. Hübers, K. Il'in, and M. Siegel, "Superconducting single-photon detector for the visible and infrared spectral range," *Journal of Modern Optics*, vol. 51, no. 9–10, pp. 1459–1466, Jan. 2004.

[35] A. D. Semenov, P. Haas, B. Günther, H.-W. Hübers, K. Il'in, and M. Siegel, "Energy Resolution of a Superconducting Nanowire Single-Photon Detector," *Journal of Low Temperature Physics*, vol. 151, no. 1–2, pp. 564–569, Jan. 2008.

[36] A. J. Kerman, E. a. Dauler, J. K. W. Yang, K. M. Rosfjord, V. Anant, K. K. Berggren, G. N. Gol'tsman, and B. M. Voronov, "Constriction-limited detection efficiency of superconducting nanowire single-photon detectors," *Applied Physics Letters*, vol. 90, no. 10, p. 101110, 2007.

[37] A. Semenov, A. Engel, K. Il, G. Gol, and M. Siegel, "Ultimate performance of a superconducting quantum detector," *PHYSICAL JOURNAL*, vol. 178, pp. 171–178, 2003.

[38] A. Kerman, J. Yang, R. Molnar, E. Dauler, and K. Berggren, "Electrothermal feedback in superconducting nanowire single-photon detectors," *Physical Review B*, vol. 79, no. 10, p. 100509, Mar. 2009.

[39] G.R.Fowles, *Introduction to Modern Optics*, 2nd Ed. New York: Dover Publications, 1989.

[40] a. Engel, a. D. Semenov, H.-W. Hübers, K. Il'in, and M. Siegel, "Fluctuation effects in superconducting nanostrips," *Physica C: Superconductivity*, vol. 444, no. 1–2, pp. 12–18, Sep. 2006.

[41] M. Bell, a. Sergeev, V. Mitin, J. Bird, a. Verevkin, and G. Gol'tsman, "One-dimensional resistive states in quasi-two-dimensional superconductors: Experiment and theory," *Physical Review B*, vol. 76, no. 9, p. 094521, Sep. 2007.

[42] J. Kitaygorsky, J. Zhang, a. Verevkin, a. Sergeev, a. Korneev, V. Matvienko, P. Kouminov, K. Smirnov, B. Voronov, G. Gol'tsman, and R. Sobolewski, "Origin of Dark Counts in Nanostructured NbN Single-Photon Detectors," *IEEE Transactions on Appiled Superconductivity*, vol. 15, no. 2, pp. 545–548, Jun. 2005.

[43] Q. Zhao, L. Zhang, T. Jia, L. Kang, W. Xu, J. Chen, and P. Wu, "Intrinsic timing jitter of superconducting nanowire single-photon detectors," *Applied Physics B*, vol. 104, no. 3, pp. 673–678, May 2011.

[44] M. K. Akhlaghi, H. Atikian, A. Eftekharian, M. Loncar, and A. H. Majedi, "Reduced dark counts in optimized geometries for superconducting nanowire single photon detectors," *Optics Express*, vol. 20, no. 21, p. 23610, Oct. 2012.

[45] E. Bermudez, "Efficiency enhancement in superconducting nanowire single photon detectors," Delft University of Technology, 2010.

[46] J.Ekin, *Experimental Techniques for Low-Temperature Measurements: Cryostat Design, Material Properties, and Superconductor Critical-Current Testing*. New York: Oxford University Press, 2006, p. 73,235,236,465,514,519,573,574.

[47] "id-300 shprt pulse laser source." [Online]. Available: http://www.idquantique.com/images/stories/PDF/id300-laser-source/id300-specs.pdf. [Accessed: 28-Feb-2013].

[48] B. E. A. Saleh and M. C. Teich, *Fundamentals of Photonics*. New York: John Wiley & Sons, Inc., 2001.

[49] Z. Yan, A. H. Majedi, and S. Safavi-Naeini, “Physical Modeling of Hot-Electron Superconducting,” vol. 17, no. 3, pp. 3789–3794, 2007.

[50] W. Slysz, M. Wegrzecki, J. Bar, P. Grabiec, M. Górska, C. Latta, V. Zwiller, A. Pearlman, A. Cross, A. Korneev, P. Kouminov, K. Smirnov, B. Voronov, G. Gol’tsman, A. Verevkin, M. Currie, and R. Sobolewski, “Fiber-coupled quantum-communications receiver based on two NbN superconducting single-photon detectors,” *Proc. of SPIE*, vol. 5957, no. 2005, p. 59571K–59571K–10, Sep. 2005.

[51] L. Zhang, Q. Zhao, Y. Zhong, J. Chen, C. Cao, W. Xu, L. Kang, P. Wu, and W. Shi, “Single photon detectors based on superconducting nanowires over large active areas,” *Applied Physics B*, vol. 97, no. 1, pp. 187–191, May 2009.

[52] S. Miki, M. Fujiwara, M. Sasaki, B. Baek, A. J. Miller, R. H. Hadfield, S. W. Nam, and Z. Wang, “Large sensitive-area NbN nanowire superconducting single-photon detectors fabricated on single-crystal MgO substrates,” *Applied Physics Letters*, vol. 92, no. 6, p. 061116, 2008.

[53] A. J. Kerman, E. a. Dauler, W. E. Keicher, J. K. W. Yang, K. K. Berggren, G. Gol’tsman, and B. Voronov, “Kinetic-inductance-limited reset time of superconducting nanowire photon counters,” *Applied Physics Letters*, vol. 88, no. 11, p. 111116, 2006.

[54] K. Ohashi, J. Fujikata, T. Ishi, D. Okamoto, K. Makita, and K. Nishi, “Development and applications of a Si nano-photodiode with a surface plasmon antenna,” vol. 6352, no. 2006, p. 63521U–63521U–9, Sep. 2006.

[55] A. Eftekharian, H. Atikian, and A. H. Majedi, “Plasmonic superconducting nanowire single photon detector,” vol. 21, no. 3, pp. 3043–3054, 2013.

[56] F. Marsili, V. B. Verma, J. a. Stern, S. Harrington, a. E. Lita, T. Gerrits, I. Vayshenker, B. Baek, M. D. Shaw, R. P. Mirin, and S. W. Nam, “Detecting single infrared photons with 93% system efficiency,” *Nature Photonics*, vol. 7, no. 3, pp. 210–214, Feb. 2013.

[57] E. a. Dauler, B. S. Robinson, a. J. Kerman, J. K. W. Yang, E. K. M. Rosfjord, V. Anant, B. Voronov, G. Gol’tsman, and K. K. Berggren, “Multi-Element Superconducting Nanowire Single-Photon Detector,” *IEEE Transactions on Applied Superconductivity*, vol. 17, no. 2, pp. 279–284, Jun. 2007.

[58] E. Dauler, M. Stevens, B. Baek, R. Molnar, S. Hamilton, R. Mirin, S. Nam, and K. Berggren, “Measuring intensity correlations with a two-element superconducting nanowire single-photon detector,” *Physical Review A*, vol. 78, no. 5, p. 053826, Nov. 2008.

[59] E. a. Dauler, A. J. Kerman, B. S. Robinson, J. K. W. Yang, B. Voronov, G. Goltsman, S. a. Hamilton, and K. K. Berggren, “Photon-number-resolution with sub-30-ps timing using multi-

element superconducting nanowire single photon detectors,” *Journal of Modern Optics*, vol. 56, no. 2–3, pp. 364–373, Jan. 2009.